J. Fluid Mech. (2024), *vol.* 1000, A57, doi:10.1017/jfm.2024.940

Linear stability analysis of a vertical liquid film over a moving substrate

Fabio Pino[1,2,†], **Miguel A. Mendez**[1] **and Benoit Scheid**[2]

[1]EA Department, The von Kármán Institute for Fluid Dynamics, 1640 Sint Genesius Rode, Belgium

[2]Transfers, Interfaces and Processes (TIPs), Université libre de Bruxelles, 1050 Brussels, Belgium

(Received 27 December 2023; revised 10 September 2024; accepted 10 September 2024)

The stability of liquid-film flows is essential in many industrial applications. In the dip-coating process, a liquid film forms over a substrate extracted at a constant speed from a bath. We studied the linear stability of this film considering different thicknesses $\hat{h}$ for four liquids, spanning an extensive range of Kapitza numbers (Ka). By solving the Orr–Sommerfeld eigenvalue problem with the Chebyshev–Tau spectral method, we calculated the threshold between growing and decaying perturbations, investigated the instability mechanism, and computed the absolute/convective threshold. The instability mechanism was studied by analysing the perturbations' vorticity distribution and the kinetic energy balance. It was found that liquids with low Ka (e.g. corn oil, $Ka = 4$) are stable for a smaller range of wavenumbers compared with liquid with high Ka (e.g. liquid zinc, $Ka = 11\,525$). Surface tension has a stabilising and a destabilising effect. For long waves, it curves the vorticity lines near the substrate, reducing the flow under the crests. For short waves, it fosters vorticity production at the interface and creates a region of intense vorticity near the substrate. In addition, we discovered that the surface tension contributes to both the production and dissipation of perturbation's energy depending on the Ka number. Regarding the absolute/convective threshold, we identified a window in the parameter space where unstable waves propagate throughout the entire domain (indicating absolute instability). Perturbations affecting Derjaguin's solution ($\hat{h} = 1$) for $Ka < 17$ and the Landau–Levich–Derjaguin solution ($\hat{h} = 0.945 Re^{1/9} Ka^{-1/6}$), are advected by the flow (indicating convective instability).

Key words: absolute/convective instability, thin films

---

1. Introduction

The linear stability analysis of film-flow solutions predicts whether small disturbances grow or decay in the long term. This is particularly important in the dip-coating industrial

---

† Email address for correspondence: fabio.pino@vki.ac.be

process, where growing disturbances make the coating layer uneven, reducing the quality of the final product (Scriven 1988). The dip-coating process consists in applying a thin film of protective material over a solid substrate (Weinstein & Ruschak 2004), with applications ranging from food industry (Suhag *et al.* 2020), e.g. coating composed of hydrophilic polymers dissolved in water (Jose, Pareek & Radhakrishnan 2020), to corrosion-protection material, e.g. zinc coating in hot-dip galvanisation Kuklík & Kudlacek (2016, Chapter 2). The substrate is coated by dipping and then withdrawing it from a liquid bath. Thereby, a liquid film forms on the substrate surface, which then solidifies into a protective layer. The thickness of this liquid film $\bar{h}$ depends on the withdrawal velocity U_p and the action of external control actuators.

In the uncontrolled case, known as free-coating or drag-out problem (Wilson 1982), $\bar{h}$ depends on the ratio between viscous drag forces over surface tension forces at the free surface (capillary number $Ca = U_p\mu/\sigma$). For small Reynolds numbers (Re), $\bar{h}$ is given by the Landau–Levich–Derjaguin (LLD) solution for $Ca \ll 1$ (Derjaguin 1943; Landau & Levich 1988) and by the Derjaguin (1944) solution for $Ca \gg 1$. Both solutions define a monotonically non-decreasing relation between $\bar{h}$ and U_p with thicker films for faster substrates. This contrasts with industrial needs aiming at thin films and fast substrates. To this end, in industrial lines, external actuators are used to remove the liquid excess from the film, e.g. impinging gas jets in the hot-dip galvanisation (Buchlin 1997; Gosset & Buchlin 2006), allowing the thickness of the coating to be controlled regardless of the substrate velocity (Mendez *et al.* 2021).

Tu & Ellen (1986) and Gosset (2007) studied the stability properties of the controlled liquid film, finding that the cutoff wavenumber is $\propto \bar{h}^2 Re^{1/2} Ca^{1/2}$. They solved the Orr–Sommerfeld eigenvalue problem with an asymptotic long-wave expansion at $O(k)$, valid for small Reynolds numbers (Benjamin 1957; Yih 1991). Other authors relied on integral boundary layer models to extend the analysis to larger Re and short wavelengths. Ivanova *et al.* (2022) found that the cutoff wavenumber is $\propto \bar{h}^{3/2} Re^{1/2} Ca^{1/6}$, whereas Barreiro-Villaverde *et al.* (2023) showed that the film is more stable to three-dimensional (3-D) than to two-dimensional (2-D) disturbances. The disagreement between the Orr–Sommerfeld approximated long-wave solution and integral models suggests that a more thorough analysis of the full Orr–Sommerfeld eigenvalue problem is required, which is still absent from the literature.

An essential aspect of unstable perturbations is the physical mechanism leading to their growth. For a falling liquid film, asymptotic (Smith 1990), vorticity and energy arguments (Kelly *et al.* 1989) showed that the motion induced by a small perturbation of the liquid film's free surface feeds the perturbation's energy by the work of shear stresses at the free surface. The extracted energy is stored in the disturbance's kinetic and potential surface tension energy. Understanding the growth mechanism in dip-coating conditions would shed some light on the role of substrate motion.

Another significant result given by the linear stability analysis is the threshold between absolutely and convectively unstable film flows (Kalliadasis *et al.* 2011, Subsection 7.1.2). Knowing this threshold is essential for the design of control actions, which can affect the whole liquid film or only a part of it (Pier 2003). The liquid film's impulse response can produce waves propagating along the flow direction (convectively unstable flow) or everywhere in the domain (absolutely unstable flow). Experiments (Liu, Paul & Gollub 1993), analytical and numerical works (Brevdo *et al.* 1999) proved that the falling film is convectively unstable, and the suspended film is absolutely unstable (Sterman-Cohen, Bestehorn & Oron 2017). Between these two extremes, a critical inclination angle defines the threshold between absolute and convective film flows (Brun *et al.* 2015; Scheid, Kofman & Rohlfs 2016; Pino, Scheid & Mendez 2024). Likewise, a critical liquid-film thickness in dip coating defines the absolute/convective (AC) threshold (Pino, Mendez & Scheid 2024). For small coating thicknesses, the entrainment due to the substrate motion sweeps the instabilities upwards; for large coating thicknesses, the gravitational effects push the instability downwards. For intermediate coating thicknesses, gravity and viscous entrainment should compensate for each other, resulting in a window of absolute instability. Knowing the position of this window in the parameters space is essential for the design of control laws, which can affect the liquid film downstream, upstream or everywhere. Despite its implications, this remains an open question that has not yet been answered and which we address theoretically in this paper.

This work studies the stability of controlled and uncontrolled liquid-film-flow solutions over a substrate moving against gravity. Given the wide variety of coating liquids, going from vegetable oils (Sharmin *et al.* 2015) to liquid metals, this analysis focuses on four liquids with a ratio of surface tension forces to inertial forces (Kapitza number Ka) in the range between $Ka \sim O(1)$ and $Ka \sim O(10^4)$. We solve the Orr–Sommerfeld eigenvalue problem via the Chebyshev–Tau spectral method (Ortiz 1969; Lanczos 1988; Johnson 1996, Chapter VII) and compare the neutral stability conditions for different values of non-dimensional film thickness. Based on the Orr–Sommerfeld solution, we calculate the components of the energy balance equations and compute the AC threshold. Although this holds in linear analysis, it is worth noting that nonlinear mechanisms may affect the spanwise development of initial perturbations, as observed by Barreiro-Villaverde *et al.* (2023) in a coating film and by Ledda *et al.* (2021) in an inverted film with calcium carbonate deposition.

The rest of the article is organised as follows. The problem set-up is described in § 2, and a description of the scaling quantities is given in § 2.1. Section 2.2 reports the governing equations, the eigenvalue problem formulation and the instability energy balance equation. The numerical implementation is reported in § 3 with methods used to solve the Orr–Sommerfeld problem, calculate the energy balance equation and search the AC threshold. Results are presented in § 5 with the stability curves, the perturbation's energy budget and the AC instability threshold. Conclusions and perspectives are given in § 6.

2. Problem description

We consider a 2-D liquid film with density ρ, dynamic viscosity μ, kinematic viscosity ν and surface tension σ, over a vertical substrate moving against gravity g at constant speed U_p. Table 1 reports the physical properties of the four liquids considered in this work: liquid zinc, water, water–glycerol solution (glycerol concentration 45 % by volume) and corn oil. These cover a broad range of conditions encountered in dip or slot coating (Gosset, Mendez & Buchlin 2019; Barreiro-Villaverde *et al.* 2023). Figure 1(*a*) shows the fixed reference system ($\mathscr{O}xy$) with x aligned with the plate and pointing in the direction of the gravitational acceleration, y along the wall-normal direction towards the free-surface, with the origin $\mathscr{O}$ on an arbitrary point of the substrate, given the translational invariance of the problem.

2.1. *Scaling quantities*

For a given liquid, the two control parameters of the systems are the substrate velocity U_p and the liquid-film thickness h. We define as reference velocity U_p and as

Liquid	ρ (kg m^{-3})	μ (mPa s)	σ (mN m^{-1})	*Ka*	*Re*
Corn oil	1023	87.5	32	4	1–180
Water–glycerol solution	1120	8.1	65.4	195	4–616
Water	1000	1	72.8	3400	10–1659
Liquid zinc	6570	3.5	700	11 525	14–2272

Table 1. Properties of the four liquids considered in the analysis (density, dynamic viscosity and surface tension from left to right), Kapitza number (*Ka*) and range of Reynolds numbers (*Re*) for substrate velocity $U_p \in [0.1, 3]$ m s^{-1} for the four liquids considered in the analysis.

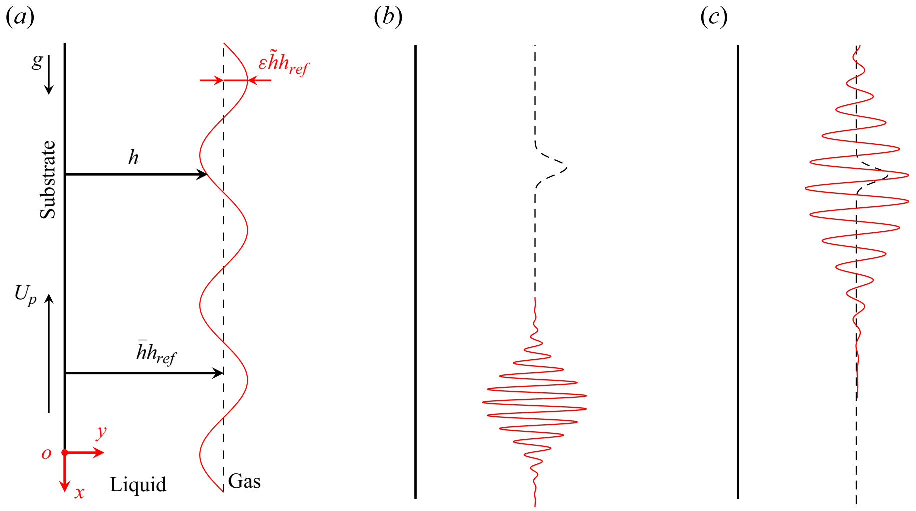

Figure 1. (*a*) Schematic of the investigated configuration with a vertical liquid film over a substrate moving with velocity U_p, where the dimensional liquid-film height h can be scaled by h_{ref} and decomposed into a dimensionless base state $\bar{h}$ and a dimensionless harmonic perturbation $\tilde{h}$ of $O(1)$, with $\varepsilon \ll 1$. Liquid-film response (red continuous curve) of a (*b*) convectively and (*c*) absolutely unstable base state solution to an initial pulse (black dashed line).

reference length the film thickness resulting from the steady-state viscous-gravity balance (see Mendez *et al.* 2021):

$$u_{ref} = U_p, \quad h_{ref} = \sqrt{\frac{\nu U_p}{g}}, \tag{2.1a,b}$$

where the subscript '*ref*' denotes reference quantities. We define the capillary length ℓ_c, relating gravity and surface tension, and the viscous length ℓ_ν, relating gravity and viscosity, as

$$\ell_c = \sqrt{\frac{\sigma}{\rho g}}, \quad \ell_\nu = \sqrt[3]{\frac{\nu^2}{g}}. \tag{2.2a,b}$$

Based on velocity and length scales in (2.1), the dependent and independent variables are scaled accordingly:

$$(u, v) \rightarrow u_{ref}(\hat{u}, \hat{v}), \quad (x, y) \rightarrow h_{ref}(\hat{x}, \hat{y}), \quad h \rightarrow h_{ref}\hat{h}, \tag{2.3a}$$

$$t \rightarrow \frac{h_{ref}}{u_{ref}}\hat{t}, \quad p \rightarrow p_{\infty} + \rho g h_{ref}\hat{p}, \tag{2.3b}$$

where the hat $\hat{\cdot}$ denotes the non-dimensional quantities and p_{∞} the atmospheric pressure. To make the non-dimensional thickness $\hat{h}$ independent of U_p and to have a clearer understanding of the role of the control parameters, we introduce another non-dimensional film thickness $\breve{h}$ based on ℓ_ν:

$$h \rightarrow \ell_\nu \breve{h}. \tag{2.4}$$

The non-dimensional groups arising from our scaling are the Reynolds number:

$$Re = \frac{u_{ref} h_{ref}}{\nu} = \sqrt{\frac{U_p^3}{g\nu}}, \tag{2.5}$$

which is equivalent to the Froude number defined as

$$F = \frac{u_{ref}^2}{g h_{ref}} = \sqrt{\frac{U_p^3}{g\nu}}. \tag{2.6}$$

This means that *Re* represents the ratio of inertia over viscous forces and the ratio between inertia and gravitational forces. The other non-dimensional group is the inverse of the capillary number defined as the ratio between surface tension and gravity:

$$Ca^{-1} = \frac{\sigma}{u_{ref}\mu} = \frac{Ka}{Re^{2/3}}, \tag{2.7}$$

where *Ka* is the Kapitza number defined as

$$Ka = \frac{\sigma}{\rho g^{1/3} \nu^{4/3}}. \tag{2.8}$$

Based on these non-dimensional groups, the non-dimensional capillary and viscous wavenumbers read

$$k_{\ell_c} = \frac{2\pi}{\hat{\ell}_c} = \frac{2\pi Re^{1/3}}{Ka^{1/2}}, \quad k_{\ell_\nu} = \frac{2\pi}{\hat{\ell}_\nu} = 2\pi Re^{1/3}. \tag{2.9a,b}$$

Using the scaling in (2.1), the Derjaguin (1944) flat film solution corresponds to $\hat{h} = 1$ and the LLD solution (Derjaguin 1943; Landau & Levich 1988; Snoeijer *et al.* 2008) corresponds to

$$\mathring{h} = 0.945 Ca^{1/6}. \tag{2.10}$$

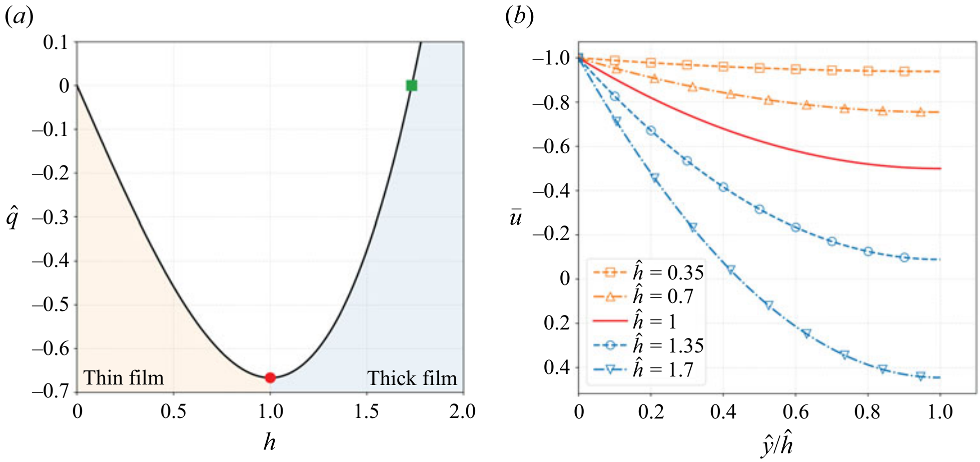

Figure 2. (*a*) Relation between the non-dimensional liquid film $\hat{h}$ and flow rate $\hat{q}$ with the Derjaguin solution (red circle), the maximum thickness $\hat{h} = \sqrt{3}$ (green square) and the thin film (orange shadowed) and thick film (blue shadowed) regions with (*b*) the associated velocity profiles.

2.2. *Mathematical formulation*

The liquid film is governed by the incompressible 2-D Navier–Stokes equations, with a velocity vector $\boldsymbol{v} = (u(x, y), v(x, y))$ and a pressure field $p(x, y)$. The equations are accompanied by the non-slip condition at the substrate $\boldsymbol{v}(x, y = 0) = (-U_p, 0)$ and a set of kinematic and dynamic boundary conditions at the free surface $(y = h)$, accounting for the continuity of the interface, and the normal and tangential force balance (see Kalliadasis *et al.* 2011, Chapter 2). The non-dimensional steady-state solutions (base states) are given by a flat interface $(\hat{h} = \bar{h})$ and the following velocity and pressure fields:

$$\bar{u}(\hat{y}) = -\tfrac{1}{2}\hat{y}^2 + \bar{h}\hat{y} - 1, \quad \bar{v}(\hat{y}) = 0, \quad \bar{p}(\hat{y}) = 0, \tag{2.11a–c}$$

where $\bar{\cdot}$ denotes the base state quantities. The balance between wall shear stress and gravity, along with the imposed velocity at the boundary, produce a non-monotonic relation between non-dimensional flow rate $\hat{q} = q/(u_{ref}h_{ref})$ and $\hat{h}$:

$$\bar{q} = \tfrac{1}{3}\bar{h}^3 - \bar{h}. \tag{2.12}$$

As shown in figure 2(*a*), this relation entails two branches of steady-state solutions: a thin one $(\bar{h} < 1)$ (orange area) and a thick one $(\bar{h} > 1)$ (blue area) with the Derjaguin's solution (red dot) and the solution $\bar{h} = \sqrt{3}$ (green square) defining the limit of zero net flow rate, above which we enter the falling film regime, i.e. for $\bar{h} > \sqrt{3}$. Figure 2(*b*) shows the non-dimensional streamwise velocity profile $\bar{u}(\hat{y})$ associated with Dejarguin's solution (continuous red line) and the thin (orange) and thick (blue) film solution (lines with markers).

To analyse the stability of the base states given by (2.11), we decompose the dependent variables as follows:

$$\hat{u} = \bar{u} + \varepsilon\tilde{u}, \quad \hat{v} = \bar{v} + \varepsilon\tilde{v}, \quad \hat{p} = \bar{p} + \varepsilon\tilde{p}, \quad \hat{h} = \bar{h} + \varepsilon\tilde{h}, \tag{2.13a–d}$$

where $\tilde{\cdot}$ represents the perturbations of $O(1)$ and $\varepsilon \ll 1$ a small parameter. Inserting (2.13) into the governing equations with the kinematic and dynamic boundary conditions and collecting the term at $O(\varepsilon)$ yields the linearised perturbation (Navier–Stokes) equations:

$$\partial_{\hat{x}}\tilde{u} + \partial_{\hat{y}}\tilde{v} = 0, \tag{2.14a}$$

$$Re(\partial_{\hat{t}}\tilde{u} + \bar{u}\partial_{\hat{x}}\tilde{u} + \tilde{v}D\bar{u}) = -\partial_{\hat{x}}\tilde{p} + \nabla^2\tilde{u}, \tag{2.14b}$$

$$Re(\partial_{\hat{t}}\tilde{v} + \bar{u}\partial_{\hat{x}}\tilde{v}) = -\partial_{\hat{y}}\tilde{p} + \nabla^2\tilde{v}, \tag{2.14c}$$

where $D(\cdot) = \partial_{\hat{y}}(\cdot)$ is the wall-normal differential operator. The boundary conditions at the substrate ($\hat{y} = 0$) reads

$$\tilde{u} = \tilde{v} = 0, \tag{2.15}$$

and, at the free surface ($\hat{y} = \hat{h}$),

$$\tilde{v} = \partial_{\hat{t}}\tilde{h} + \bar{u}\partial_{\hat{x}}\tilde{u}, \tag{2.16a}$$

$$\tilde{p} = 2\partial_{\hat{y}}\tilde{v} - Ca^{-1}\partial_{\hat{x}\hat{x}}\tilde{h}, \tag{2.16b}$$

$$\tilde{h} = \partial_{\hat{y}}\tilde{u} + \partial_{\hat{x}}\tilde{v}. \tag{2.16c}$$

We concatenate the streamwise $\tilde{u}$ and cross-stream $\tilde{v}$ perturbations, by recasting (2.14) in terms of the stream function $\varPsi$ defined as

$$\tilde{u} = \partial_{\hat{y}}\varPsi, \quad \tilde{v} = -\partial_{\hat{x}}\varPsi, \tag{2.17a,b}$$

and assuming a normal mode solution of the form

$$\varPsi = \varphi(\hat{y})\exp(\mathrm{i}(k\hat{x} - \omega\hat{t})), \quad \tilde{h} = \eta\exp(\mathrm{i}(k\hat{x} - \omega\hat{t})), \tag{2.18a,b}$$

where $\varphi(\hat{y}) = \varphi_r(\hat{y}) + \mathrm{i}\varphi_i(\hat{y})$ and η are the amplitudes of the stream function and the film thickness, respectively, $k = k_r + \mathrm{i}k_i$ is the wavenumber, $\omega = \omega_r + \mathrm{i}\omega_i$ the angular frequency, and $c = c_r + \mathrm{i}c_i = \omega/k$ is the perturbation's complex phase speed. This yields the following Orr–Sommerfeld eigenvalue problem:

$$\boldsymbol{OS}(k, c, Re)\varphi(\hat{y}) = [\boldsymbol{A}(k, Re) - c\boldsymbol{B}(k, Re)]\varphi(\hat{y}) = 0, \tag{2.19}$$

where $\boldsymbol{A}(k, Re)$ is given by

$$\boldsymbol{A}(k, Re) = (D^2 - k^2)^2 - \mathrm{i}\,Re\,k[\bar{u}(D^2 - k^2) + 1] \tag{2.20}$$

and $\boldsymbol{B}(k, Re) = \partial_c\boldsymbol{OS}(k, c, Re)$ is given by

$$\boldsymbol{B}(k, Re) = -\mathrm{i}\,Re\,k(D^2 - k^2), \tag{2.21}$$

with boundary conditions $\boldsymbol{OS}_{BC}\varphi|_{0,\hat{h}} = 0$ defined as

$$\varphi(0) = D\varphi(0) = 0, \tag{2.22a}$$

$$\eta = \varphi(\hat{h})/(c - a), \tag{2.22b}$$

$$[(D^2 - 3k^2) + \mathrm{i}\,Re\,k(c - a)]D\varphi(\hat{h}) - \mathrm{i}\eta\,Ca^{-1}\,k^3 = 0, \tag{2.22c}$$

$$(D^2 + k^2)\varphi(\hat{h}) - \eta = 0, \tag{2.22d}$$

where $a = \bar{u}(\bar{h}) = (\bar{h}^2/2 - 1)$ is the base-state velocity at the interface.

The solution of the eigenvalue problem sets a relation between the wavenumber k and angular frequency ω. This is known as the dispersion relation and depends on three parameters:

$$\mathscr{D}(\omega, k; Re, Ka, \bar{h}) = 0. \tag{2.23}$$

These solutions are linked to the system's response to a local impulse, known as Green's function (Brevdo *et al.* 1999; Schmid & Henningson 2001, pp. 270–271). It can be shown that these are the system's poles (Charru 2011, p. 97) and, thus, control whether a disturbance grows or vanishes.

The analysis of poles for varying ω with a fixed k is known as a temporal analysis, whereas the analysis of poles for varying k and fixed ω is known as a spatial analysis. The images of any straight lines $k_i = C$, where C is an arbitrary constant, are called temporal branches in the complex frequency space, whereas the images of any straight line $\omega_i = E$, where E is an arbitrary constant, are called spatial branches in the complex wavenumber space (Kupfer, Bers & Ram 1987). The points of intersection of spatial branches are called spatial branch points.

For a real k, a base state is classified as temporally stable or unstable, depending on the value of the growth rate (ω_i): a state is unstable if $\omega_i > 0$, as this results in the unbounded temporal growth of infinitesimal perturbation, whereas it is stable if $\omega_i < 0$, as this results in the return of the perturbed liquid film to its steady-state equilibrium conditions for all k. The locus of points with zero growth rate ($\omega_i = 0$) corresponds to the neutral curve, with neither amplified nor damped perturbations.

A base state is absolutely unstable if the solution with zero group velocity $c_g = \partial\omega/\partial k = 0$ has $\omega_i > 0$ (Gaster 1968; Charru 2011). The condition $c_g = 0$ is equivalent to $\partial\omega_r/\partial k_r = \partial\omega_i/\partial k_r = 0$ or, because of the Cauchy–Riemann relation, to $\partial\omega_i/\partial k_i = \partial\omega_r/\partial k_i = 0$. Since both ω_r and ω_i must also satisfy the Laplace equation in the wavenumber domain k for a differentiable (holomorphic) $\omega(k)$, this implies that the condition $c_g = \partial\omega/\partial k = 0$ corresponds to a saddle point in the wavenumber domain k. However, not all saddle points are admissible; we return to this point in § 3.2.

3. Methodology

3.1. *Numerical solution of the eigenvalue problem*

Before presenting the numerical methods used to solve the Orr–Sommerfeld problem, we remove η from the boundary conditions (2.22), substituting the kinematic condition (2.22*b*) into the shear stress balance (2.22*d*) and the original shear stress balance (2.22*d*) into the normal stress balance (2.22*c*) (Pelisson Chimetta, Hossain & de Moraes Franklin 2018). The Orr–Sommerfeld eigenvalue problem (2.19) with the modified boundary conditions is solved using the Chebyshev–Tau spectral method (Johnson 1996; Canuto *et al.* 2012, Section. 3.1). The eigenfunction $\varphi(\hat{y})$ is approximated with a combination of $N + 1$ Chebyshev polynomials of the first kind, with the coefficients a_i being collected in the vector $\boldsymbol{\phi} = [a_0, a_1, \ldots, a_N]^{\mathrm{T}}$. The approximated eigenfunction is introduced in (2.19), and the residual is projected onto another base of Chebyshev polynomials of the first kind. This results in an algebraic system of $N + 1$ equations representing a generalised eigenvalue problem with eigenvector ϕ and eigenvalue c:

$$(\mathsf{A}(Re, k) - c\mathsf{B}(Re, k))\phi = 0, \tag{3.1}$$

with matrices A and B representing the discretisation of the operators $\boldsymbol{A}$ in (2.20) and $\boldsymbol{B}$ in (2.21). Replacing the last four rows of the system in (3.1) with the modified boundary conditions (Boyd 2001, Section 6.4) leads to the generalised eigenvalue problem:

$$\hat{A}(Re, k)\phi = c\hat{B}(Re, k)\phi, \tag{3.2}$$

with $\hat{A}$ and $\hat{B}$ representing matrices A and B in (3.1) with the enforced boundary conditions. The eigenvalue problem is solved using Python's function *numpy.linalg.eig*. The approximation error decreases as the magnitude of the four τ coefficients is reduced Lanczos (1988, Chapter 7, § 12).

To cope with the spurious eigenvalues (Dawkins, Dunbar & Douglass 1998; Bourne 2003), we solve (3.2) for $N = 20$ and $N = 80$, retaining the eigenvalues whose difference in magnitude, using the Euclidean norm ($\|\cdot\|$), is below 0.1 (Gardner, Trogdon & Douglass 1989). Among these, that with the largest growth rate $\omega_{i1}^1 = c_{i1}^1/k$ (most unstable) is selected. To further improve the computational accuracy of the associated eigenvector ϕ_1^1, we run 10 iterations of the inverse power method (Trefethen & Bau 2022, Lecture 27):

$$\phi^{j+1} = \frac{(C - I/c_1)^{-1}\phi_1^{\{j\}}}{||(C - I/c_1)^{-1}\phi_1^{\{j\}}||}, \tag{3.3}$$

where $j \in \{1, 2, \ldots, 9\}$ is the iteration count and $C = \hat{A}^{-1}\hat{B}$. We defined C in this way, with the inverse of $\hat{A}$ rather than the inverse of $\hat{B}$, because $\hat{B}$ is always singular.

Given Ka and $\hat{h}$, to compute the neutral stability curves in the k–Re space with $k \in \mathbb{R}$, we start from the long-wave most-unstable mode ((ϕ_1, c_1) with the largest c_i), with $k^{\{1\}} = 3.5 \times 10^{-6}$, and we march it along the discrete k axis running 20 iterations of Rayleigh quotient iteration at every point $k^{\{j\}}$ and collecting the values of $c^{\{j\}}$:

$$\phi_1^{\{j+1\}} = \frac{(C - I/c_1^{(j)})\phi_1^{\{j\}}}{||(C - 1/c_1^{\{j\}})^{-1}\phi_1^{\{j\}}||}, \quad I/c_1^{\{j+1\}} = \frac{\phi_1^{*\{j+1\}}C\phi_1^{\{j+1\}}}{\phi_1^{*\{j+1\}}\phi_1^{\{j+1\}}}, \tag{3.4a,b}$$

where $\cdot^*$ denotes complex conjugate. Thereby, converting c_i into ω_i, we find the growth rate as a function of k. The zero of this curve k_f ($k \in \mathbb{R} : \omega_i(k) = 0 \wedge k \neq 0$), also known as the cutoff frequency, belongs to the neutral curve. The neutral curve is constructed by repeating this procedure varying Re.

3.2. *Numerical method for zero group-velocity perturbation*

To assess whether a base state is absolutely or convectively unstable, we follow Brigg's method (outlined in Schmid & Henningson 2001, Subsection 7.2.2). This consists of mapping the complex k space into the complex ω space, identifying the saddle points, and checking *a posteriori* if these respect the causality condition using the collision criterion (Briggs 1964; Huerre & Monkewitz 1985; Thual, Thual & Dewitte 2013; Avanci, Rodríguez & Alves 2019). According to this criterion, the only valid saddle points arise as spatial branch points, pinching two spatial branches coming from the positive and negative half-planes of the complex wavenumber space. Depending on the value of the growth rate in these points, the base state is convectively ($\omega_i < 0$) or absolutely ($\omega_i > 0$) unstable.

Given a set of parameters (Re, Ka, $\hat{h}$), we explore a portion of the complex wavenumber space $k_i \in [k_{i_{min}}, k_{i_{max}}]$ and $k_r \in [k_{r_{min}}, k_{r_{max}}]$, discretised with a uniform mesh of $M \times M$

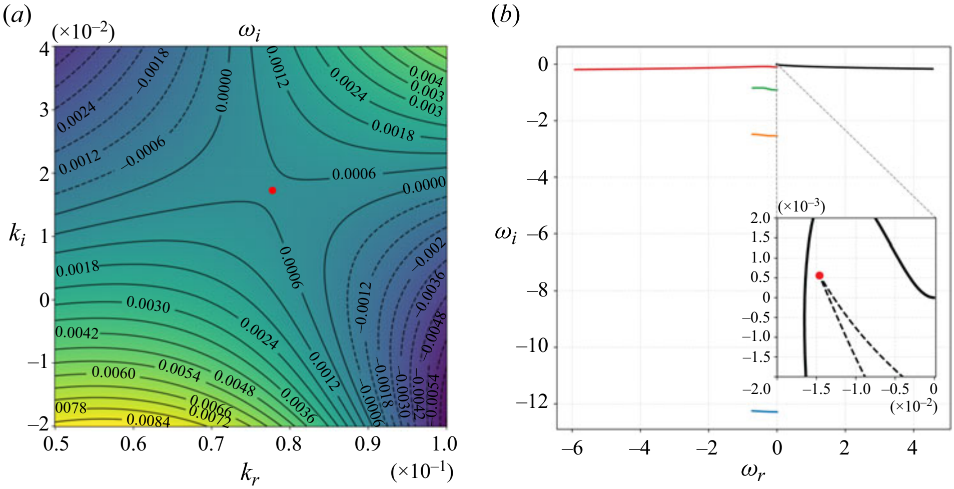

Figure 3. Position of the saddle point (red dot) for the zinc with $\hat{h} = 0.8885$, $Re = 30$ (*a*) in the complex k space with the colourmap of ω_i and (*b*) in the complex frequency space with the cusp (black dashed line) and the spatial branches of the first four modes (coloured lines), sorted by ascending values of ω_i, obtained solving the Orr–Sommerfeld problem along the path $k_i = 0$ in the complex wavenumber space.

elements with spacing Δk_i and Δk_r. Starting from the most-unstable mode (ϕ_1, c_1), obtained solving the Orr–Sommerfeld problem (3.2) for a given pair $(k_r^{\{1\}}, k_i^{\{1\}})$, we march over the discretised wavenumber space running 20 iterations of Rayleigh quotient iteration (3.4) at every point $(k_r^{\{j\}}, k_i^{\{j\}})$ and collecting the values of $c^{\{j\}}$. The solution at one point of the grid serves as a starting point for the computation of the solution in the adjacent one. We march over the wavenumber space with a spiral matrix algorithm to avoid two consecutive steps falling outside the iterative method's convergence region. Given the computed mapping $\omega_r(k_r, k_i)$, $\omega_i(k_r, k_i)$, we calculate the saddle point location using numerical differentiation and checking the collision condition.

Figure 3(*a*) presents an example of the mapping, with ω_i colour plot and contour map as a function of k, along with the position of the saddle point (red point). To check whether the collision criterion is satisfied, we check the position of the saddle point in the complex ω space. Figure 3(*b*) shows the saddle point position (red dot) in the complex ω space and the temporal branches of the first five modes (coloured lines), sorted by ascending values of ω_i, along the path $k_i = 0$. The collision criterion is respected if the saddle point is surmounted by an odd number of spatial branches (Kupfer *et al.* 1987; Suslov 2006).

To determine the AC instability threshold (saddle point with $\omega_i = 0$), we explore the parameter spaces (Ka–Re) and ($\hat{h}$–Re). We fix Re and run a line search along the other parameter. A detailed pseudocode description is reported in Appendix A.

4. Energy balance and mechanism of the unstable perturbation

To understand the onset mechanism of unstable perturbations, we solve the linearised Navier–Stokes equations via a long-wave asymptotic expansion up to $O(k^2)$ in § 4.1. In addition, to gain a deeper insight into the growth mechanism of unstable perturbations for any k, we derive the kinetic energy balance for the perturbations in § 4.2.

4.1. *Mechanism of long-wave instability in a moving reference frame*

We consider a solution of (2.14) with boundary conditions (2.15) and (2.16) in the form of normal modes given by

$$\tilde{u} = \acute{u}(\hat{y})\exp(\mathrm{i}k(\hat{x}-c\hat{t})), \quad \tilde{v} = \acute{v}(\hat{y})\exp(\mathrm{i}k(\hat{x}-c\hat{t})), \tag{4.1a}$$

$$\tilde{h} = \eta\exp(\mathrm{i}k(\hat{x}-c\hat{t})), \quad \tilde{p} = \acute{p}(\hat{y})\exp(\mathrm{i}k(\hat{x}-c\hat{t})), \tag{4.1b}$$

where the $\acute{\cdot}$ denotes the amplitudes. We consider a reference system moving with the substrate velocity U_p ($\hat{u} = -1$), with the change of variables:

$$\acute{u}_m(\hat{y}) = \acute{u}(\hat{y}) + 1, \quad c_m = c + 1, \quad \bar{u}_m(\hat{y}) = \bar{u}(\hat{y}) + 1 = -\frac{y^2}{2} + \hat{h}\hat{y}, \tag{4.2a–c}$$

where $\acute{u}_m$, c_m and $\bar{u}_m$ are the streamwise velocity amplitude, the phase speed and the base state velocity in the moving reference frame. We seek an approximated solution via long-wave expansion of the amplitudes and the phase speed up to $O(k)$ (Benjamin 1957; Yih 1963; Smith 1990):

$$\acute{u}_m = \acute{u}_{m0} + \acute{u}_{m1}k + O(k^2), \quad \acute{v} = \acute{v}_0 + \acute{v}_1 k + O(k^2), \quad \acute{p} = \acute{p}_0 + \acute{p}_1 k + O(k^2), \tag{4.3a}$$

$$\eta = \eta_0 + \eta_1 k + O(k^2), \quad c_m = c_{m0} + c_{m1}k + O(k^2), \tag{4.3b}$$

with the normalisation $\eta_0 = 1$ and $\eta_1 = 0$. Collecting the terms at $O(1)$ gives the system

$$D\acute{v}_0(\hat{y}) = 0, \quad \acute{v}_0(\hat{y})D\bar{u}_m(\hat{y})Re = D^2\acute{u}_{m0}(\hat{y}), \quad D\acute{p}_0(\hat{y}) = D^2\acute{v}_0(\hat{y}), \tag{4.4a–c}$$

with boundary conditions

$$\acute{u}_{m0}(0) = 0, \quad \acute{v}_0(0) = 0, \tag{4.5a}$$

$$\acute{p}_0(\hat{h}) = 2\acute{v}_0(\hat{h}), \quad \acute{v}_0(\hat{h}) = 0 \quad D\acute{u}_{m0}(\hat{h}) = 1. \tag{4.5b}$$

At $O(k)$, we obtain the system

$$\acute{v}_1(\hat{y}) + \mathrm{i}(\acute{u}_{m0}(\hat{y}) - 1) = 0, \tag{4.6a}$$

$$-Re(\acute{u}_{m0}(\hat{y}) - 1)(c_{m0} - \bar{u}_m(\hat{y}) + 1) + \acute{p}_0(\hat{h}) - \mathrm{i}\,Re\,\acute{v}_1(\hat{y})D\bar{u}_m(\hat{y}) + \mathrm{i}D^2\acute{u}_{m1}(\hat{y}) = 0, \tag{4.6b}$$

$$-\mathrm{i}c_{m0}\,Re\,\acute{v}_0(\hat{y}) + D\acute{p}_1(\hat{y}) + \mathrm{i}\,Re\,\bar{u}_m(\hat{y})\acute{v}_0(\hat{y}) - \mathrm{i}\,Re\,\acute{v}_0(\hat{y}) - D\acute{v}_1(\hat{y}) = 0, \tag{4.6c}$$

with the boundary conditions

$$\acute{u}_1(0) = 0 \quad \acute{v}_1(0) = 0, \tag{4.7a}$$

$$\acute{v}_1(\hat{h}) = -\mathrm{i}(c_{m0} - \bar{u}_m(\hat{h}) + 1), \tag{4.7b}$$

$$\acute{p}_1(\hat{y}) - 2D\acute{v}_1(\hat{h}) = 0, \quad D\acute{u}_{1m}(\hat{h}) + \mathrm{i}\acute{v}_0(\hat{h}) = 0. \tag{4.7c}$$

The solution of these systems is presented in § 5.2.

4.2. *Energy balance of the perturbation*

To study the instability mechanism, we analyse the contributions to the perturbation's kinetic energy equation as in Kelly *et al.* (1989) and Lin (1970). This equation is obtained by summing up the product of (2.14*b*) by $\tilde{u}$ and of (2.14*c*) by $\tilde{v}$, averaging over a wavelength λ, integrating over the liquid-film thickness $\hat{h}$ and then using (2.14*a*) and the boundary conditions (2.15) and (2.16*c*) to obtain

$$\mathrm{RKINE} + \mathrm{SURTE} = \mathrm{SHEST} + \mathrm{REYNS} + \mathrm{DISSI}, \tag{4.8a}$$

with

$$\mathrm{RKINE} = \frac{1}{2\lambda}\frac{\mathrm{d}}{\mathrm{d}t}\int_0^{\lambda}\int_0^{\hat{h}}(\tilde{u}^2+\tilde{v}^2)\,\mathrm{d}\hat{y}\,\mathrm{d}\hat{x}, \tag{4.8b}$$

$$\mathrm{SURTE} = -\frac{Ca^{-1}}{Re\,\lambda}\int_0^{\lambda}[\tilde{v}|_{\hat{h}}(\partial_{\hat{x}\hat{x}}\tilde{h})]\,\mathrm{d}\hat{x}, \tag{4.8c}$$

$$\mathrm{SHEST} = \frac{1}{Re\,\lambda}\int_0^{\lambda}\tilde{u}|_{\hat{h}}(\partial_{\hat{y}}\tilde{u}|_{\hat{h}}+\partial_{\hat{x}}\tilde{v}|_{\hat{h}})\,\mathrm{d}\hat{x}, \tag{4.8d}$$

$$\mathrm{REYNS} = -\frac{1}{\lambda}\int_0^{\lambda}\int_0^{\hat{h}}\tilde{u}\tilde{v}D\bar{u}\,\mathrm{d}\hat{y}\,\mathrm{d}\hat{x}, \tag{4.8e}$$

$$\mathrm{DISSI} = \mathrm{DISSI}_1 + \mathrm{DISSI}_2 + \mathrm{DISSI}_3. \tag{4.8f}$$

The terms on the left-hand side represent the energy stored in the perturbation in the form of kinetic (RKINE) and surface tension potential (SURTE) energies. The terms on the right-hand side represent the energy extracted from the base state through the work of shear stress at the interface (SHEST), Reynolds stress (REYNS) and dissipative viscous effects (DISSI). DISSI encompass the contribution of extensional (DISSI_1 and DISSI_3) and shear terms (DISSI_2), given by

$$\mathrm{DISSI}_1 = -\frac{1}{Re\,\lambda}\int_0^{\lambda}\int_0^{\hat{h}}2(\partial_{\hat{x}}\tilde{u})^2\,\mathrm{d}\hat{y}\,\mathrm{d}\hat{x}, \tag{4.9a}$$

$$\mathrm{DISSI}_2 = -\frac{1}{Re\,\lambda}\int_0^{\lambda}\int_0^{\hat{h}}\upsilon^2\,\mathrm{d}\hat{y}\,\mathrm{d}\hat{x}, \tag{4.9b}$$

$$\mathrm{DISSI}_3 = -\frac{1}{Re\,\lambda}\int_0^{\lambda}\int_0^{\hat{h}}2(\partial_{\hat{y}}\tilde{v})^2\,\mathrm{d}\hat{y}\,\mathrm{d}\hat{x}, \tag{4.9c}$$

where $\upsilon = \partial_{\hat{y}}\tilde{u} + \partial_{\hat{x}}\tilde{v}$ is proportional to the strain rate. The perturbation quantities are given by

$$\tilde{u} = (D\varphi_r\cos(\theta) - D\varphi_i\sin(\theta))E, \tag{4.10a}$$

$$\tilde{v} = k(\varphi_i\cos(\theta) + \varphi_r\sin(\theta))E, \tag{4.10b}$$

$$(\partial_{\hat{y}}\tilde{u} + \partial_{\hat{x}}\tilde{v}) = [(D^2+k^2)(\varphi_r\cos(\theta) - \varphi_i\sin(\theta)]E, \tag{4.10c}$$

$$\tilde{\omega} = [(D^2-k^2)(\varphi_r\cos(\theta) - \varphi_i\sin(\theta)]E, \tag{4.10d}$$

$$\tilde{h} = (\eta_r\cos(\theta) - \eta_i\sin(\theta))E, \tag{4.10e}$$

with

$$\theta = k(x - c_r t), \quad E = \exp(kc_i t), \quad \tilde{\omega} = \partial_{\hat{y}}\tilde{u} - \partial_{\hat{x}}\tilde{v}, \tag{4.11a–c}$$

where $\tilde{\omega}$ is the perturbation vorticity.

Using the kinematic condition (2.22*b*), the real η_r and imaginary η_i parts of surface deflection are given by

$$\eta_r = (\varphi_r(\hat{h})\hat{c} + \varphi_i(\hat{h})c_i)/(\hat{c}^2 + c_i^2), \tag{4.12a}$$

$$\eta_i = (\varphi_i(\hat{h})\hat{c} - \varphi_r(\hat{h})c_i)/(\hat{c}^2 + c_i^2), \tag{4.12b}$$

where $\hat{c} = c_r - a$. To have an accurate computation of the terms in (4.8*a*), we calculate the integral along $\hat{x}$ analytically and along $\hat{y}$ numerically, using the Simpson's rule over a grid of 10^4 equispaced points in the range $[0, \hat{h}]$ such that the difference in magnitude between the right-hand side and the left-hand side of (4.8*a*) is below 1 % of the kinetic energy (RKINE) (Lin, Lian & Creighton 1990).

5. Results and discussion

In this section, we report the results of the linear stability analysis in terms of neutral curves and growth rates (§ 5.1), instability mechanism (§ 5.2) and AC threshold (§ 5.3) for the fluids in table 1. Moreover, we compute the threshold for the Derjaguin's flat film solution ($\hat{h} = 1$) in the (Ka–Re) parameter space.

The Orr–Sommerfeld eigenvalue problem (2.19) is solved using $N = 20$ Chebyshev polynomials in the approximation of the stream function amplitude, and a grid spacing for the saddle point search of $\Delta k_r = 2.5 \times 10^{-4}$ and $\Delta k_i = 3 \times 10^{-4}$ (see Appendix B.1). To verify our implementation, we compare the dispersion relations and the eigenfunctions against a long-wave asymptotic expansion of the Orr–Sommerfeld problem up to the third order in k (see Appendix B.2).

5.1. *Neutral stability curves and growth rates*

First, we compare the neutral stability curves given by the numerical solution of the Orr–Sommerfeld problem and by analytical representation. These representations are obtained by calculating the zeros of the long-wave approximation obtained in Appendix B.1, i.e. cancelling $c_1^\star$ in (B5), leading to the expression

$$k = \sqrt{\frac{2}{5}\frac{\hat{h}^3}{Ka}Re^{5/3}}, \tag{5.1}$$

for an expansion up to $O(k)$ with the surface tension correction at leading order ($Ca^{-1}k^2 = O(1)$), and to the expression

$$k = \frac{24\sqrt{15015}\hat{h}^{3/2}\sqrt{Re}}{\sqrt{2\,427\,904\hat{h}^{11}Re^3 + 45\,463\,275\hat{h}^5 Re + 21\,621\,600\dfrac{Ka}{Re^{2/3}}}}, \tag{5.2}$$

for an expansion up to $O(k^3)$ without correction. Figure 4 shows the approximated neutral curves and the one obtained with the spectral methods for $\hat{h} \in [0.2, 0.5, 0.8]$ considering (*a*) zinc ($Ka = 11\,525$) and (*b*) water ($Ka = 3400$). The instability region lies between the curve and the $k = 0$ axis. The analytical expressions agree with the numerics for small

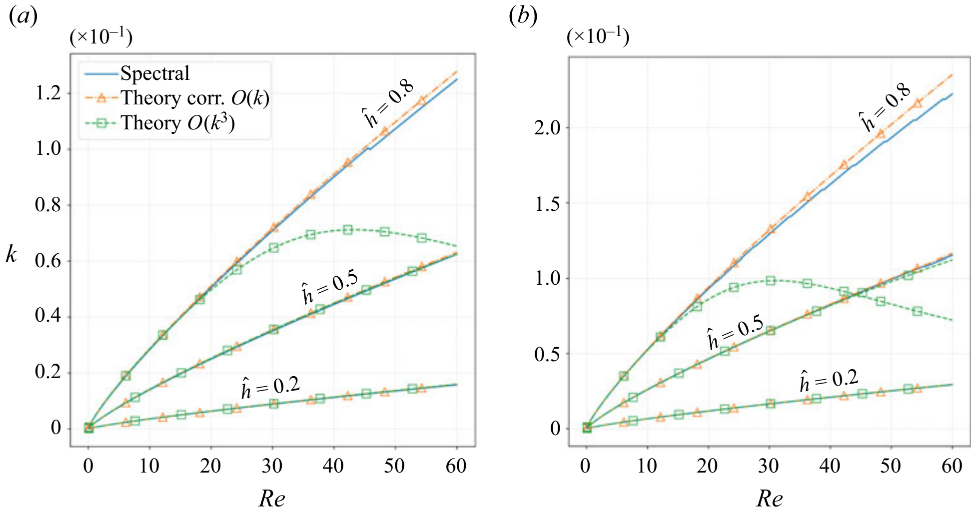

Figure 4. Neutral curves separating the region of stable (above) and unstable (below) wavenumbers, based on asymptotic expansions with surface tension correction up to $O(k)$ (orange dash-dotted line with triangles) and without correction up to $O(k^3)$ (green dashed line with squares), against the numerical ones (continuous blue line), for $\hat{h} \in [0.2, 0.5, 0.8]$ with (*a*) zinc ($Ka = 11\,525$) and (*b*) water ($Ka = 3400$).

values of $\hat{h}$. The solution with correction agrees better than the full third-order solution, which highlights the validity of the assumption $Ca^{-1} \times k^2 = O(1)$ for large Ka and small $\hat{h}$.

Going into more depth in the analysis of the neutral curves and the dispersion relations, figures 5 and 6 show the numerical neutral curves for different values of $\hat{h}$ and the dispersion relations with axes normalised with the maximum value of ω_i ($\max(\omega_i)$) and the cutoff wavenumber k_m at $Re = 30$ for the four liquids. The wavenumber k_{max} and the magnitudes $\omega_{i,max}$ of the growth rate peaks are reported in table 2. For $\hat{h} \leq 1$, ω_i gradually increases with k, up to the peak, then sharply decreases towards k_m. For $\hat{h} > 1$, ω_i reaches the peak after a steep increase, and then it gently reaches k_m.

As for the growth rate, $\hat{h}$ also influences the neutral stability curves. For the four fluids, the instability region enlarges for large $\hat{h}$ and small Ka, with curves progressively gathering around the same wavenumbers for thick film conditions ($\hat{h} > 1$), with the limit case of corn oil ($Ka = 4$), where the neutral curves are almost superimposed. Similar behaviour is also visible in the dispersion relations. As Ka decreases, the relative distance between the peaks' positions for $\hat{h} > 0.35$ shrinks, with the limit case of corn oil ($Ka = 4$) where the curves for $\hat{h} = 0.4$ and $\hat{h} = 1$ also change shapes, becoming similar to those for $\hat{h} > 1$.

This highlights stabilising mechanisms given by the balance of inertia, viscous and gravitational forces without the effect of surface tension. As Ka decreases, the stabilising effects of the surface tension diminish compared with the viscous effects. Even when increasing $\hat{h}$, the instability region does not expand much. This suggests that neutral modes with $k = O(1)$ arise as an equilibrium of mostly viscous and gravitational forces, which is not linked to the velocity of the plate. Indeed, increasing Re does not change the relative position of the neutral curves; it just brings this equilibrium point to larger k.

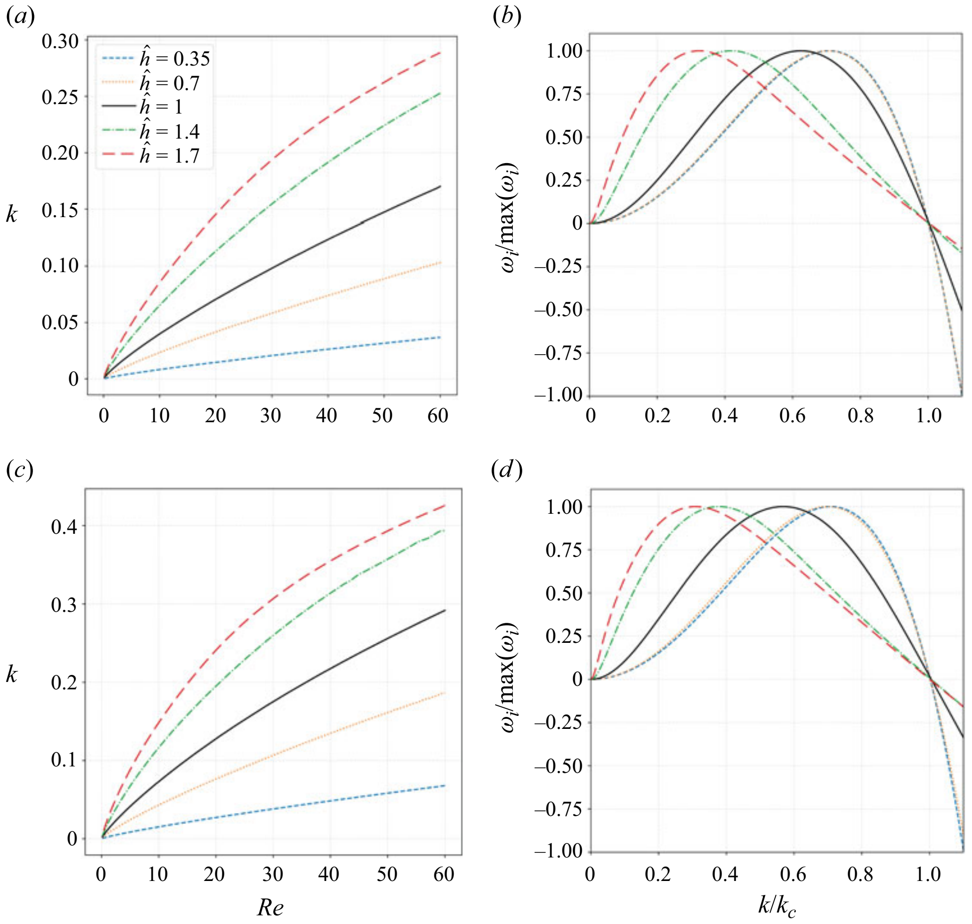

Figure 5. (*a*,*c*) Neutral curves for different values of the non-dimensional liquid-film thickness $\hat{h}$, (*b*,*d*) dispersion relations normalised with $\max(\omega_i)$ and the cutoff frequency k_c for $Re = 30$ for (*a*,*b*) liquid zinc ($Ka = 11\,525$) and (*c*,*d*) water ($Ka = 3400$).

Figure 7 shows the evolution of (*a*) the ω_i peak magnitude $\max(\omega_i)$ and (*b*) the wavenumber k_{max} varying $\hat{h}$ for the different fluids. As Ka decreases, the maximum growth rate increases. Corn oil ($Ka = 4$) has the largest growth rates of all the $\hat{h}$ with its peaks overlapping for $\hat{h} \geq 1$.

Interestingly, the peaks' locations do not have a monotonic behaviour with $\hat{h}$. For the corn oil ($Ka = 4$), the peak position advances towards smaller wavelengths for $\hat{h} = 0.7$, and then it goes to longer wavelengths for higher values of $\hat{h}$. As Ka increases, the peak is located at smaller wavenumbers, and it moves to $\hat{h} = 1.7$ passing through $\hat{h} = 1$ for the water–glycerol ($Ka = 195$) solution.

The liquid-film height $\hat{h}$ and the Kapitza number also play a role in the phase speed of the unstable perturbations. Figure 8 shows how the phase speed c_r as a function of the wavenumber k and the liquid-film height $\hat{h}$ at $Re = 30$ with a highlight on the neutral curve (continuous white line) and the positions of the maximum growth rate (white dashed line) for (*a*) liquid zinc ($Ka = 11\,525$), (*b*) water ($Ka = 3400$) and (*c*) corn oil ($Ka = 4$).

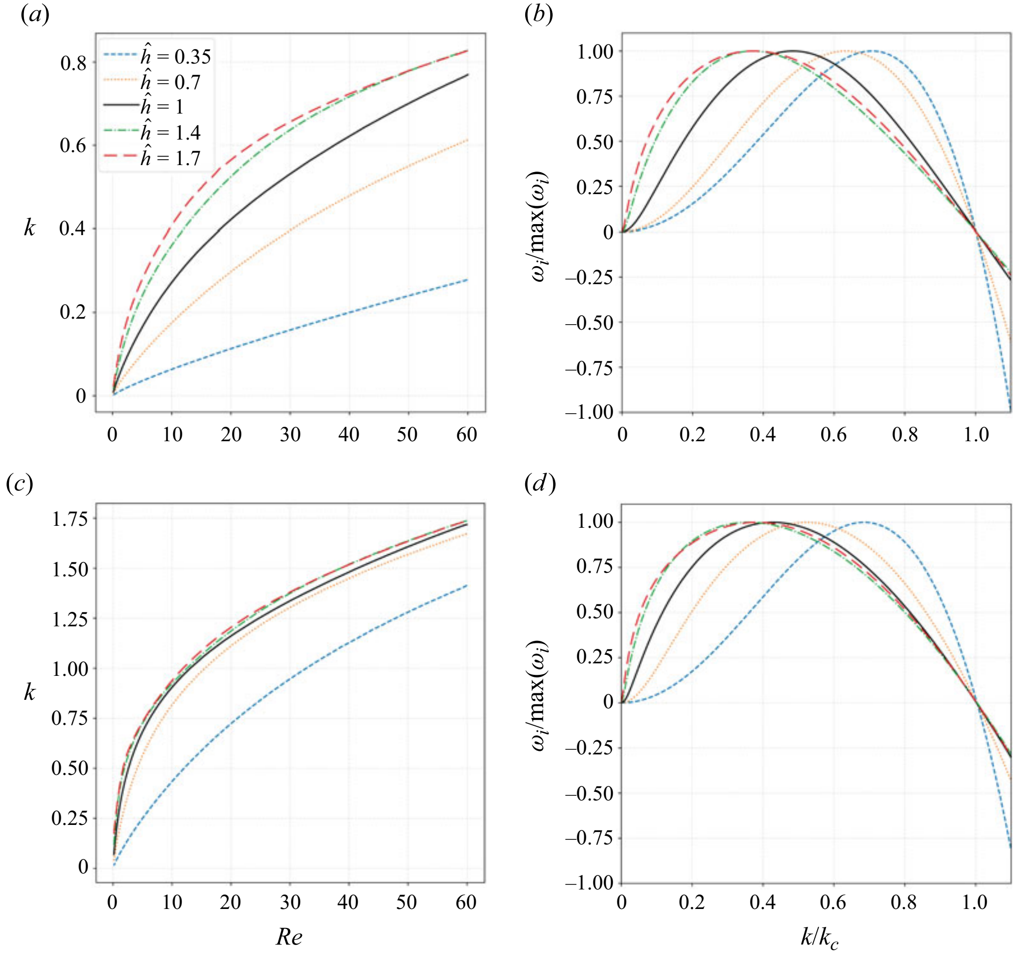

Figure 6. (a,c) Neutral curve and (b,d) dispersion relations normalised with $\max(\omega_i)$ and the cutoff frequency k_c, for $Re = 30$ and different values of $\hat{h}$, for (a,b) liquid water–glycerol ($Ka = 195$) solution and (c,d) corn oil ($Ka = 4$).

Ka	4		195		3400		11 525	
$\hat{h}$	k_{max}	$\omega_{i,max}$	k_{max}	$\omega_{i,max}$	k_{max}	$\omega_{i,max}$	k_{max}	$\omega_{i,max}$
0.35	0.65	0.0015	0.11	4.6×10^{-5}	0.027	2.7×10^{-6}	0.015	8×10^{-7}
0.7	0.69	0.033	0.25	0.011	0.075	0.0013	0.041	0.0004
1	0.57	0.049	0.26	0.029	0.1	0.011	0.061	0.0054
1.4	0.5	0.049	0.24	0.036	0.1	0.021	0.065	0.015
1.7	0.53	0.049	0.24	0.037	0.095	0.023	0.063	0.018

Table 2. Peak of growth rate $\omega_{i,max}$ and the associated wavenumber k_{max} for different liquids and $\hat{h}$ at $Re = 30$.

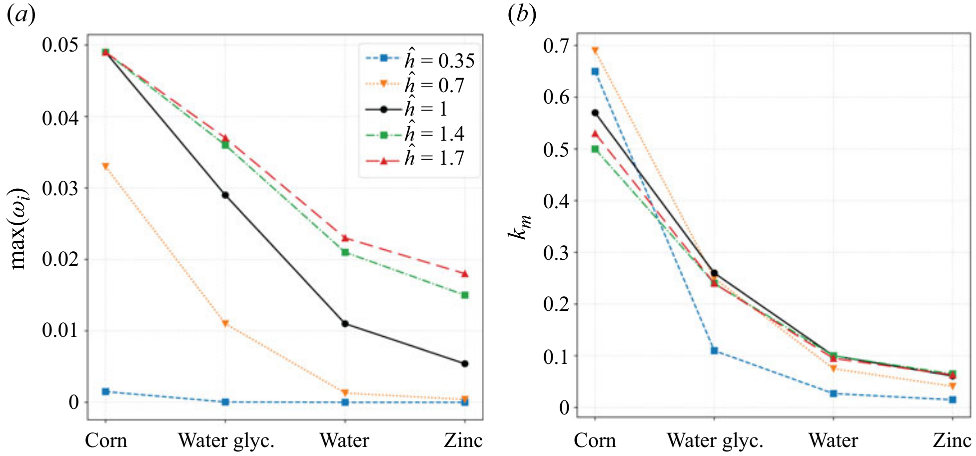

Figure 7. Values of (*a*) the maximum growth rate max(ω_i) and (*b*) the associated wavenumber k_m for different $\hat{h}$ and liquids at $Re = 30$.

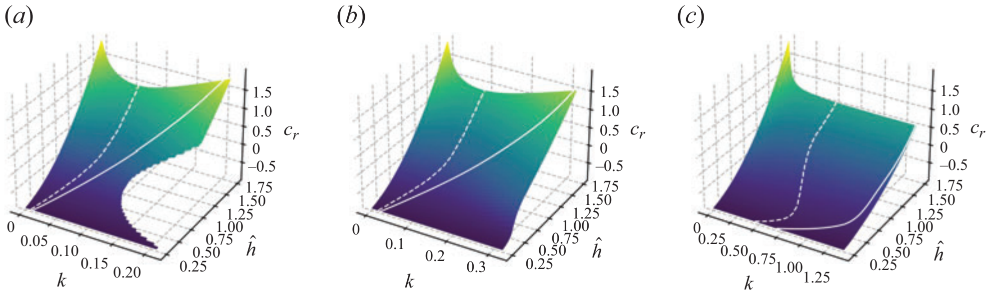

Figure 8. Coloured surface showing the real part of the phase speed c_r as a function of the wavenumber k and the flat liquid-film height $\hat{h}$ at $Re = 30$ with the neutral curve (white continuous line) and maximum growth rate (white dashed line) for (*a*) liquid zinc ($Ka = 11\,525$), (*b*) water ($Ka = 3400$) and (*c*) corn oil ($Ka = 4$).

As we move along k for a fixed $\hat{h}$, the phase speed varies first linearly (for small $\hat{h}$) and then nonlinearly (for large $\hat{h}$). This relation is quadratic for zinc ($Ka = 11\,525$) and water, with the minimum at the same wavenumber of the maximum growth rate. In contrast, for the corn oil ($Ka = 4$), after a steep variation for $k \rightarrow 0$, it becomes linear again with a minimum not coinciding with the peak of growth rate. As we move along $\hat{h}$ for a fixed k, the phase speed of long waves varies quadratically with $\hat{h}$, in accordance with the leading order approximation of the asymptotic expansion (B3) ($c_r = \hat{h}^2 - 1$). As we increase k, this approximation loses validity, with waves propagating slower. This relation tends to become linear as we move to shorter wavelengths. The slope of this relationship changes with k and Ka, becoming almost insensitive to k, in the case of corn oil ($Ka = 4$). High Ka, the most-unstable mode, travels slower than any other unstable mode.

5.2. *Long-wave mechanism and energy balance of the unstable perturbation*

In this subsection, we describe the mechanism behind the growth of unstable perturbations using momentum and vorticity arguments. Moreover, we investigate how the perturbation's energy is extracted and stored depending on the values of the non-dimensional groups and the liquid-film height, highlighting the role of viscous terms. In the falling-liquid-film case, Kelly *et al.* (1989), with the energy-based approach, and Smith (1990), with asymptotic expansions, showed that the long-wave instability is fed by a streamwise flow field resulting from the base state's shear stress deficiency at the free-surface.

5.2.1. *Long-wave instability mechanism*

Considering the harmonic disturbance $\tilde{h}$ over a flat interface $\bar{h}$ (see § 4.1), the shear stress at the perturbed interface is given by a base state and a perturbation contribution. Expanding $D\hat{u}$ around the base state thickness $\bar{h}$, we obtain, at first order,

$$D\hat{u}(\hat{h}) = D\bar{u}(\bar{h}) + D\tilde{u}(\bar{h}) + D^2\bar{u}(\bar{h})\tilde{h} = 0. \tag{5.3}$$

Since the base state is shear-free at the interface ($D\bar{u}(\bar{h}) = 0$) and knowing that $D^2\bar{u}(\bar{h}) = -1$, (5.3) reduces to

$$D\tilde{u}(\bar{h}) - \tilde{h} = 0. \tag{5.4}$$

The equilibrium of forces implies that the disturbance has to generate a positive shear stress $D\tilde{u}(\bar{h})$ to compensate for $\tilde{h}$. To analyse this mechanism, we considered a reference frame moving at the substrate velocity U_p ($\hat{u} = -1$), and we expand the streamwise velocity amplitude $\acute{u}$ in a power series of k assuming long-wave conditions (4.1) (Smith 1990). The solution at $O(1)$ of (4.4) with boundary conditions (4.5) is given by a linear velocity amplitude $\acute{u}_{m0}(\hat{y})$ and a positive phase speed c_{m0}:

$$\acute{u}_{m0}(\hat{y}) = \hat{y} + 1, \quad c_{m0} = \bar{h}^2. \tag{5.5a,b}$$

The behaviour of c_{m0} is solely determined by gravity. The thicker the base state, the more gravity is important, and the more the wave travels faster downwards along the $\hat{x}$ direction.

Figure 9(*a*) shows the flow field at leading order as a consequence of a harmonic displacement of the interface (red line). Since the flow field is in phase with the liquid-film displacement, the streamwise velocity is maximum at the peak and minimum at the trough. Considering a control volume in the range $\theta \in [0, \pi/2]$, enclosed between a peak and a node at the interface, this has a positive net flow rate. The velocity field pushes liquid to the right at the crest, with a zero flow rate at the node. In accordance with the continuity equation, this implies a positive displacement of the film interface to accommodate this accumulation of mass, leading to a travelling wave in the positive $\hat{x}$ direction. The solution of (4.6*a*) gives the normal velocity at $O(k)$:

$$v_1 = -i\hat{y}^2/2. \tag{5.6}$$

The link between the phase speed and the flow rate is given by the kinematic boundary condition at the interface (4.7*b*):

$$c_{m0} - \bar{u}_m(\hat{h}) = v_1 = \int_0^{\hat{h}} u_{m0} - 1\,\mathrm{d}\hat{y} = \hat{h}^2/2. \tag{5.7}$$

This initiating mechanism affects the development of the flow field at $O(k)$ through two *inertial stresses* in (4.6*b*):

$$-\,\mathrm{i}Re(u_{m0}(\hat{y}) - 1)(\bar{u}_m(\hat{y}) - c_{m0} - 1) \quad \text{and} \quad Re\, v_1(\hat{y})D\bar{u}_m(\hat{y}). \tag{5.8a,b}$$

The first term corresponds to the advection of the reduced leading-order solution by the base state velocity with respect to the reduced leading order wave speed. The second

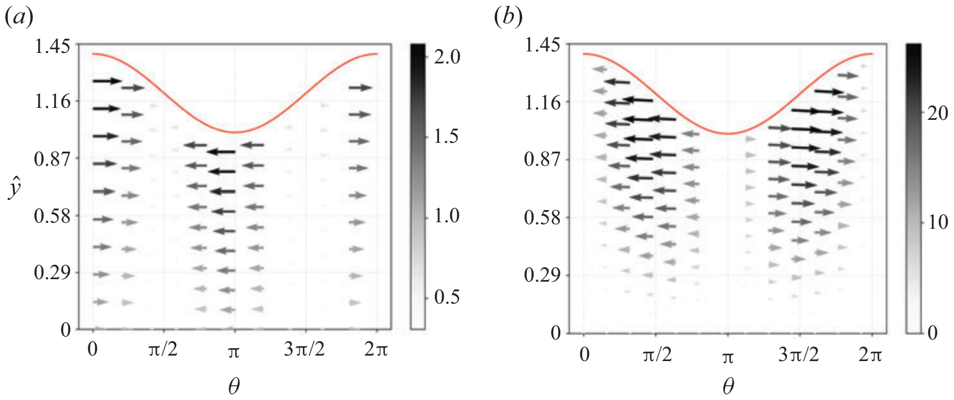

Figure 9. Magnitude (greyscale) and vector field (arrows) of the perturbation's velocity field (*a*) at leading order and (*b*) at first order in the wavenumber *k*.

term corresponds to the advection of the base state velocity by the first-order wall-normal velocity v_1. Since the phase speed c_{m0} is larger than any values in $\bar{u}_m(\hat{y})$, and being $D\bar{u}_m(\hat{y}) = -\hat{y} + \hat{h}$ positive for all $\hat{y} \in [0, \hat{h}]$, these two terms are both negative. This leads to a destabilising flow field given by the solution of the first-order equations (4.6) with boundary conditions (4.7):

$$u_{m1}(\hat{y}) = \frac{Re}{24}\mathrm{i}(8\hat{h}^4\hat{y} - 4\hat{h}^2\hat{y}^3 + 12\hat{h}\hat{y} + \hat{h}\hat{y}^4 - 4\hat{y}^3). \tag{5.9}$$

Figure 9(*b*) shows the flow field calculated with (5.9). Since the velocity amplitude $u_{m1}(\hat{y})$ is imaginary and positive, the flow has a phase shift of π/2 with respect to the wave displacement. Consequently, the velocity pushes fluid from the troughs to the peaks, sustaining the growth of the perturbation. This renders a growth mechanism based on the extraction of energy contained in the leading-order solution, which, in turn, extracts energy from the base state through the work done by the shear stress at the interface.

5.2.2. *Vorticity perturbation at the free surface and in the bulk*

In the previous subsection, we studied the general structure of the instability mechanism. The first-order solution in *k*, fed by leading-order *inertial stresses*, generates a destabilising flow from the troughs to the peaks due to a π/2 phase shift to the free-surface displacement. In this section, we go into more detail, analysing how the phase shift and the magnitude of the perturbation change with the wavenumber and the flat liquid-film height. To this end, we look at the growth of the perturbation in terms of the vorticity field. The perturbation's shear stress correction in (5.4) can be seen as a source of vorticity at the free surface ω_{FS}. We consider a reference frame moving with the wave speed c_r, i.e. $\theta = k(\hat{x} - c_r\hat{t})$, and we assume a sinusoidal displacement of the free surface:

$$\tilde{h} = \sin(\theta), \tag{5.10}$$

with $\theta = 0$ at 0, this implies through (4.12*a*), that

$$\eta_r = 0, \quad \eta_i = -1. \tag{5.11a,b}$$

By means of the kinematic boundary condition (2.22*b*), we scale the eigenfunction such that

$$\phi_r(\hat{h}) = c_i, \quad \phi_i(\hat{h}) = -\hat{c}. \tag{5.12a,b}$$

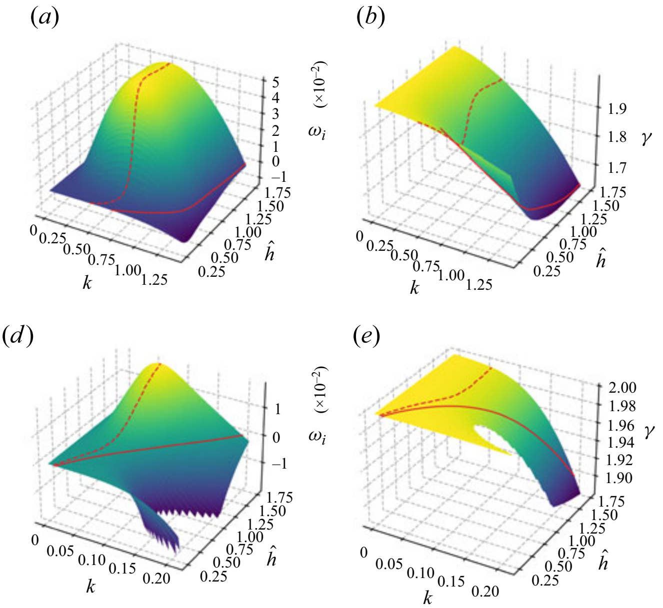

Figure 10. (a,d) Growth rate, (b,e) free-surface vorticity amplitude and (c,f) phase shift as a function of k and $\hat{h}$ with the neutral curve (continuous red line) and the positions of maximum growth rates (red dashed line) for $Re = 30$, considering (a–c) corn oil ($Ka = 4$) and (d–f) zinc ($Ka = 11\,525$).

The shear stress condition (2.22d) imposes that

$$D^2\phi_r(\hat{h}) = -k^2 c_i, \quad D^2\phi_i(\hat{h}) = -2 + k^2\hat{c}. \tag{5.13a,b}$$

By replacing these expressions in (4.10d), we obtain the vorticity at the free surface:

$$\omega_{FS} = \gamma \sin(\theta - \xi), \tag{5.14}$$

with the amplitude γ and the phase shift ξ given by

$$\gamma = 2\sqrt{(1 - k^2\hat{c})^2 + (k^2 c_i)^2]}, \quad \xi = \arctan(k^2 c_i/(1 - k^2\hat{c}). \tag{5.15a,b}$$

Depending on ξ, ω_{FS} stabilises ($\xi < 0$) or destabilises ($\xi > 0$) the free-surface displacement (Kelly *et al.* 1989).

Figure 10 shows (a,d) the growth rate ω_i, (b,e) the amplitude γ and (c,f) the phase shift ξ of the free-surface vorticity as a function of the wavenumber k and the liquid-film thickness $\hat{h}$ at $Re = 30$, with the neutral curve (continuous red line) and the maximum growth rate (dashed red line) for (a–c) the corn oil ($Ka = 4$) and (d–f) the liquid zinc ($Ka = 11\,525$). For a fixed k, ω_i gently grows with $\hat{h}$ driven by a vorticity with a large amplitude and a very small positive phase shift. For $\hat{h} = 1$, ω_i grows more sharply, accompanied by an increase in the phase shift and a decrease in the vorticity amplitude. In the corn oil ($Ka = 4$) case, the growth rate and the phase shift reach a plateau for large $\hat{h}$, in line with the saturating mechanism introduced in § 5.1. The phase shift ξ peaks at higher wavenumbers than the growth rate ω_i. The decay of the vorticity amplitude γ with k compensates for the destabilising effect of larger phase shifts, decreasing the growth rate. This suggests that the instability mechanism is also driven by the vorticity in the bulk, thus confirming the results in the previous subsections.

To investigate this behaviour, we analysed the vorticity perturbation $\tilde{\omega}(\theta,\hat{y}) = \partial_{\hat{x}}\tilde{v} - \partial_{\hat{y}}\tilde{u}$ within the liquid film. The vorticity equation is obtained by taking the curl of the momentum equations (2.14*b*) and (2.14*c*), considering the continuity equations (2.14*a*) and the base state (2.11), which leads to

$$\partial_{\hat{t}}\tilde{\omega} + \bar{u}\partial_{\hat{x}}\tilde{\omega} - \tilde{v}D^2\bar{u} = \frac{1}{Re}(\partial_{\hat{x}\hat{x}}\tilde{\omega} + D^2\tilde{\omega}). \tag{5.16}$$

Considering the reference frame moving with the wave speed c_r and knowing that $D^2\bar{u} = -1$, we obtain

$$k(\bar{u} - c_r)\partial_\theta\tilde{\omega} + \tilde{v} = \frac{1}{Re}(k^2\partial_{\theta\theta}\tilde{\omega} + D^2\tilde{\omega}). \tag{5.17}$$

On the left-hand side, the first term corresponds to the advection relative to the wave velocity, and the second term corresponds to the vorticity perturbation's advection of the base state. The term on the right-hand side corresponds to the viscous diffusion of vorticity. Inserting a normal mode solution for the vorticity with $k \in \mathbb{R}$ and $c = c_r + \mathrm{i}c_i$,

$$\tilde{\omega} = \acute{\omega}(\hat{y})\exp(\mathrm{i}k(\hat{x} - c\hat{t})) = \acute{\omega}(\hat{y})\exp(kc_i\hat{t})\exp(\mathrm{i}\theta), \tag{5.18}$$

and for the wall-normal velocity given by (4.1) in (5.17) leads to the expression for the free-surface amplitude $\acute{v}(\hat{y})$,

$$\acute{v}(\hat{y}) = \mathrm{i}k(c_r - \bar{u}(\hat{y}))\acute{\omega}(\hat{y}) + \frac{1}{Re}(-k^2 + D^2)\acute{\omega}(\hat{y}). \tag{5.19}$$

Note that for $Re \gg 1$, the relation reduces at leading order in k to

$$\acute{v}(\hat{y}) \approx \mathrm{i}k(c_r - \bar{u}(\hat{y}))\acute{\omega}(\hat{y}), \tag{5.20}$$

which corresponds to neglecting viscous effects.

Approximating c_r with the long-wave asymptotic solution at $O(1)$ in (B3), the term $c_r - \bar{u}$ is always positive $\forall \hat{y} \in [0, \hat{h}]$, implying that the vertical velocity amplitude changes linearly with the vorticity amplitude with a phase shift of $\pi/2$ along θ.

Figure 11 shows the perturbation (*a*, *b*, *c*, *g*, *h* and *i*) vorticity and (*d*, *e*, *f*, *j*, *k* and *l*) normal velocity fields at (*a–f*) $\hat{h} = 0.7$ and (*g–l*) $\hat{h} = 1.7$ for the corn oil ($Ka = 4$) with $k = 0.5$ (*a*, *d*, *g* and *j*), 0.93 (*b*, *e*, *h* and *k*) and 1.2 (*c*, *f*, *i* and *l*) with the maximum (red square) and minimum (red triangle) of vorticity at the interface with $Re = 30$. For $k = 0.5$, the vorticity contours deform towards the left, advected by the flow. Since the advection velocity strengthens, this tilting effect is more intense for large $\hat{h}$. This structure recalls the capillary separation eddy in a falling liquid film of finite amplitude in the capillary flow region (Dietze, Al-Sibai & Kneer 2009). The induced normal velocity field changes sign at the peak of vorticity along θ, leading to a positive (negative) net vertical flow rate under the crests (trough), which fosters the growth of the perturbation.

As the wavenumber increases, the vorticity lines bend towards the right near the substrate. This curvature stabilises the perturbation, enlarging the negative (positive) normal velocity area under the peak (trough). At the same time, the vorticity tends to concentrate near the free surface, approaching its maximum value at the interface and forming a boundary layer region with strong shear stresses. Despite the differences in the vorticities and normal velocities' distributions, the stability mechanism at $\hat{h} = 0.7$ and $\hat{h} = 1.7$ for the corn oil ($Ka = 4$) is very similar. As we have seen, the neutral curves and the dispersion relations (figure 6), the vorticity at the free surface (figure 10) and the order

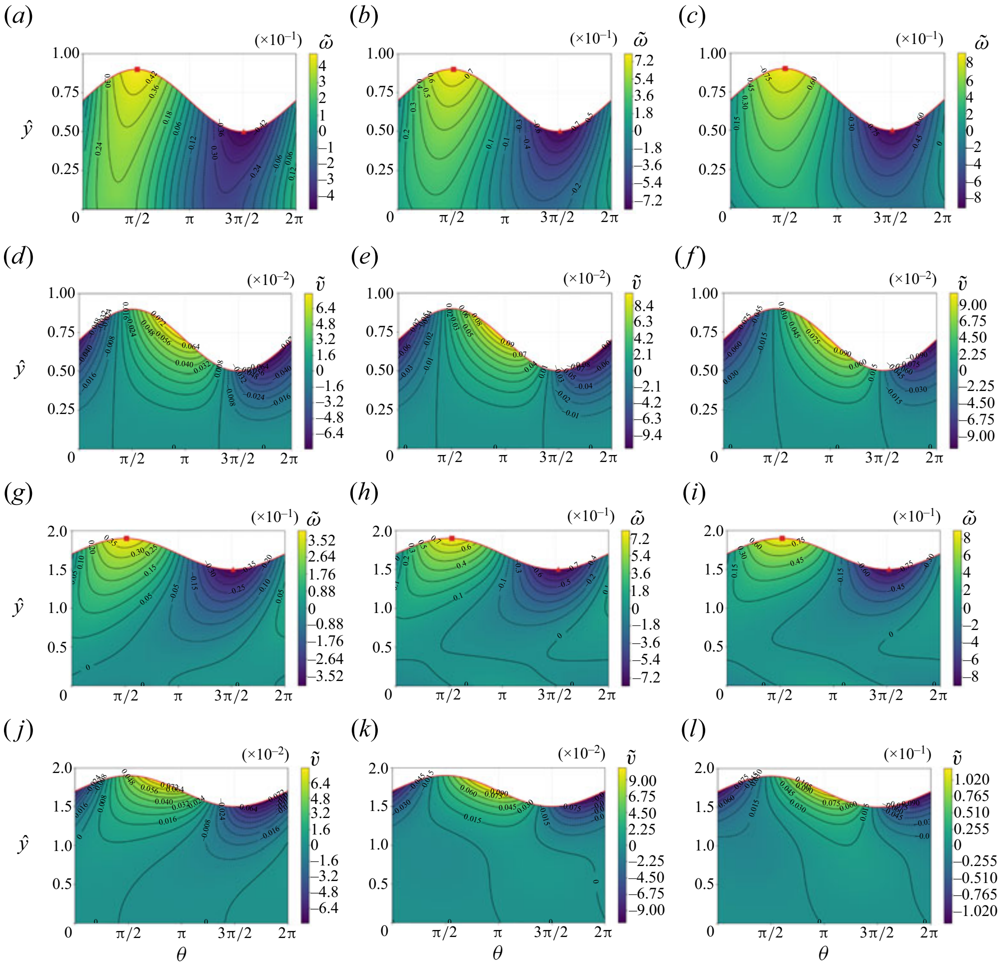

Figure 11. Perturbation (a, b, c, g, h and i) vorticity and (d, e, f, j, k and l) normal velocity fields at (a–f) $\hat{h} = 0.7$ and (g–l) $\hat{h} = 1.7$ for the corn oil ($Ka = 4$) with $k = 0.5$ (a, d, g and j), 0.93 (b, e, h and k) and 1.2 (c, f, i and l) with the maximum (red square) and minimum (red triangle) of vorticity at the interface with $Re = 30$.

of magnitude of the vorticity in bulk are almost the same for the two conditions. This means that for small Ka, the instability growth is mainly driven by the vorticity at the free surface and in its proximity.

Things change as we move to larger Ka. Figure 12 shows the perturbation (a, b, c, g, h and i) vorticity and (d, e, f, j, k and l) normal velocity fields at (a–f) $\hat{h} = 0.7$ and (g–l) $\hat{h} = 1.7$ for the liquid zinc ($Ka = 11\,525$) with k equal to (a,d) 0.002, (g,j) 0.003, (b,e) 0.047, (c,f) 0.051, (h,k) 0.077 and (i,l) 0.15 with the maximum (red square) and minimum (red triangle) of vorticity at the interface at $Re = 30$. For $\hat{h} = 0.7$, the advection has a very small effect on the vorticity contour's curvature. The viscous effects almost completely dominate the vorticity distribution. As we have seen in figure 10, for $\hat{h} = 0.7$, the instability grows mostly due to the vorticity magnitude rather than the phase shift, which is almost zero.

For $\hat{h} = 1.7$, the vorticity lines tilt in the advection direction as we increase the wavenumber. Moreover, for $k = 0.15$, a region of intense vorticity is created near the

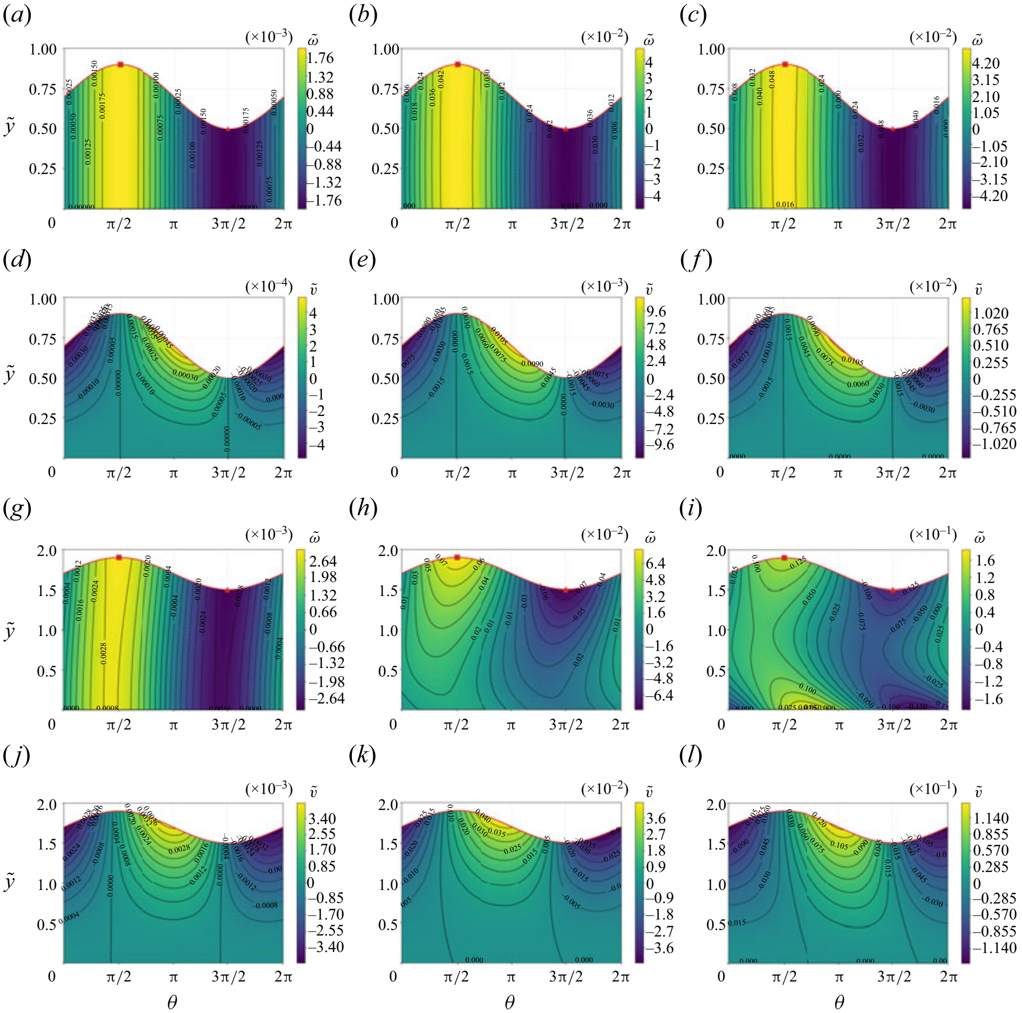

Figure 12. Perturbation (*a*, *b*, *c*, *g*, *h* and *i*) vorticity and (*d*, *e*, *f*, *j*, *k* and *l*) normal velocity fields at (*a*–*f*) $\hat{h} = 0.7$ and (*g*–*l*) $\hat{h} = 1.7$ for the liquid zinc ($Ka = 11\,525$) with k equal to (*a*,*d*) 0.002, (*g*,*j*) 0.003, (*b*,*e*) 0.047, (*c*,*f*) 0.051, (*h*,*k*) 0.077 and (*i*,*l*) 0.15 with the maximum (red square) and minimum (red triangle) of vorticity at the interface at $Re = 30$.

substrate, destabilising the flow, increasing the net flow rate under the crests, and creating a boundary layer near the substrate in addition to that near the free surface.

This region is the product of the streamwise pressure gradient induced by the surface tension. The normal vorticity flux at the substrate, also known as *vorticity source strength* (Lighthill 1963), is given by(Morton 1984)

$$-\partial_{\hat{y}}\omega = \partial_{\hat{x}}\tilde{p} - 1, \tag{5.21}$$

where the right-hand side represents the rate of vorticity production per unit area and comprises the perturbation's streamwise pressure gradient and the gravitational effect. Positive vorticity is generated when the streamwise pressure gradient outweighs the gravitational effect.

For small k, the pressure is constant a long $\hat{y}$, with the most-sensitive zone to the surface tension close to the substrate. As we have shown in Appendix B.2, for high Ka, the surface tension influences the first-order solution for small k. The first-order streamwise velocity amplitude, derived by differentiating the stream function (B5) with respect to the wall-normal coordinate, is given by

$$\acute{u}_1 = D\varphi_1^{\star}(\hat{y}) = \frac{\mathrm{i}\hat{y}^2}{12}(\hat{h}\,Re\,\hat{y}^2 - 4\hat{h}^2 Re\hat{y} + 12k^2\,Ca). \tag{5.22}$$

Assuming $\hat{h} = O(1)$, the surface tension term is dominant for small $\hat{y}$ i.e. near the substrate.

Moreover, the surface tension also increases the vorticity near the free surface (figure 12*e* and *f*). The normal vorticity flux at the interface is given by (Dietze *et al.* 2009; Wu 1995)

$$-\partial_{\hat{n}}\tilde{\omega} = \frac{\partial_{\hat{x}}\tilde{p}}{\sqrt{1+(\partial_{\hat{x}}\tilde{h})^2}}, \tag{5.23}$$

where $\hat{n}$ is the non-dimensional normal vector to the interface pointing toward the liquid. As for the substrate flux, it depends on the streamwise pressure gradient. At a peak (trough) location, the pressure gradient in the streamwise direction is negative (positive), so the film produces positive (negative) vorticity at the free surface.

The mechanism leading to the formation of this boundary layer zone is as follows: the pressure imposed by the surface tension pushes fluid down (up) at the crests (troughs), which, via the continuity equation, produces a positive (negative) streamwise flow near the substrate. The movement of the substrate increases the shear effects compared with the falling film case, leading to more intense vorticity regions.

These outcomes highlight the importance of Ka, even for long-wave perturbation (small k). This means that surface tension is crucial for stabilising short waves and storing perturbation energy and for the early development of instability and vorticity distribution in liquid film. Moreover, we reveal two mechanisms of instability involving viscous stresses associated with the boundary layer at the free surface for the corn oil ($Ka = 4$) and the boundary layer at the substrate for the zinc ($Ka = 11\,525$).

5.2.3. *Energy balance of the perturbation*

We have analysed the early stages of the long-wave instability mechanism and how the vorticity at the free surface and in bulk fosters the growth of unstable perturbations. Here, we study the terms forming the kinetic energy balance (4.8*a*) of an unstable perturbation, as presented in § 4.2.

The vorticity near the substrate also affects the dissipation terms defined in (4.8*f*) and (4.9). Figure 13 shows the elongational (DISSI_1 green dashed-dotted line with circles and DISSI_3 orange dashed line with triangles) and shear (DISSI_2 blue dashed line with squares) stresses contributing to the total dissipative viscous effects (DISSI_{tot} red continuous line) as a function of k at $\hat{h} = 1.7$ and $Re = 30$ for (*a*) corn oil ($Ka = 4$) and (*b*) liquid zinc ($Ka = 11\,525$). Here DISSI_1 is equal to DISSI_3 due to the continuity equation. For small k, DISSI_2, which is a function of the strain rate υ, dominates the dissipative effects, with DISSI_1 and DISSI_2 slowly increasing with k. For larger k, DISSI_2 decreases in magnitude. At $Ka = 4$ (corn oil), it decreases monotonically with k, whereas for $Ka = 11\,525$ (zinc), it reaches a minimum and increases again towards the cutoff wavenumber. This is due to the creation of a boundary layer near the substrate. Near the

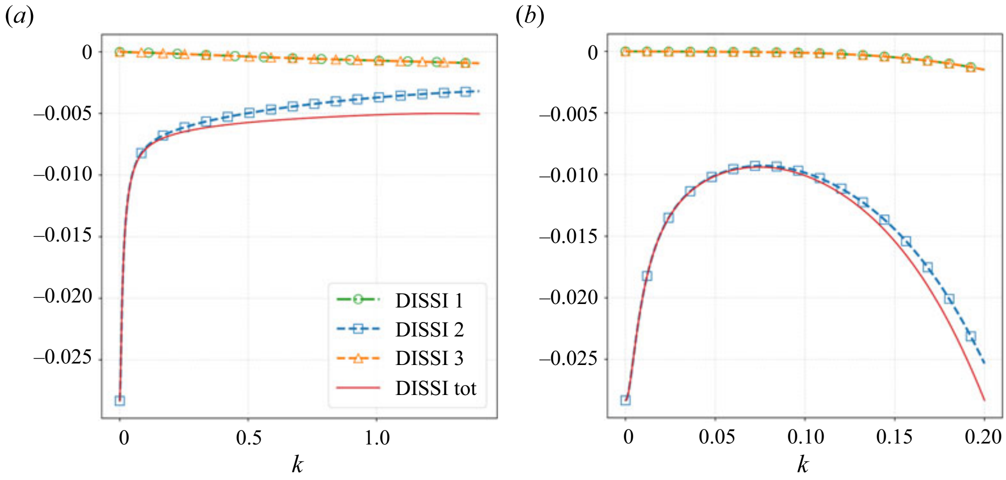

Figure 13. Distribution of the extensional stresses DISSI_1 and DISSI_3 and shear stress DISSI2, with $\hat{h} = 1.7$ and $Re = 30$ for (*a*) the corn oil ($Ka = 4$) and (*b*) the liquid zinc ($Ka = 11\,525$).

boundary, the strain rate υ is equal to the vorticity, and they are both generated with the same boundary flux densities (Morton 1984). In addition to the boundary, the bulk is also a source of strain rate. The equation governing the strain rate is given by

$$\partial_{\hat{t}}\upsilon = -2\partial_{\hat{x}\hat{y}}\tilde{p} + \frac{1}{Re}(\partial_{\hat{x}\hat{x}}\upsilon + \partial_{\hat{y}\hat{y}}\upsilon). \tag{5.24}$$

When the surface tension induces a pressure gradient in the liquid film, the bulk also generates a strain rate, feeding DISSI_2.

5.3. *Absolute/convective (AC) threshold*

The previous subsections focused on the instability mechanism using long-wave expansions, vorticity and energy arguments. In this subsection, we further extend our analysis of unstable perturbations of Pino, Mendez & Scheid (2024), calculating the AC threshold in the $\hat{h}$–Re and c_r–Re parameter spaces with the LLD solution $\mathring{h}$, the real part of the wavenumber k_r (red empty triangles) and the non-dimensional capillary length $\hat{\ell}_c$ defined in (2.9) (blue continuous line with empty squares), for the liquids in table 1. Moreover, we calculate the threshold also in the Ka–Re space for the Derjaguin solution ($\hat{h} = 1$). The region of absolute instability is depicted as a shaded area bounded by the AC threshold simulated points (continuous black line with black circles).

In the literature on falling films, Brevdo *et al.* (1999) showed that a flat liquid film over a vertical substrate is always convectively unstable due to gravitational effects. In the case of an inclined substrate, the hydrostatic effects compensate for the gravity, leading to regions of absolute instability (Brun *et al.* 2015; Scheid *et al.* 2016). Similarly, the leading actors in the moving substrate case are gravity, inertia, viscosity and surface tension. For certain parameters, these compensate for each other, leading to regions of absolute instability.

5.3.1. *AC threshold in the Ka–Re space with* $\hat{h} = 1$

Figure 14 shows the AC threshold for the Derjaguin solution ($\hat{h} = 1$) in (*a*) the Ka–Re parameter space, with the trend line $Ka = 0.15Re^{1.8}$ (red dashed line) and in (*b*) the

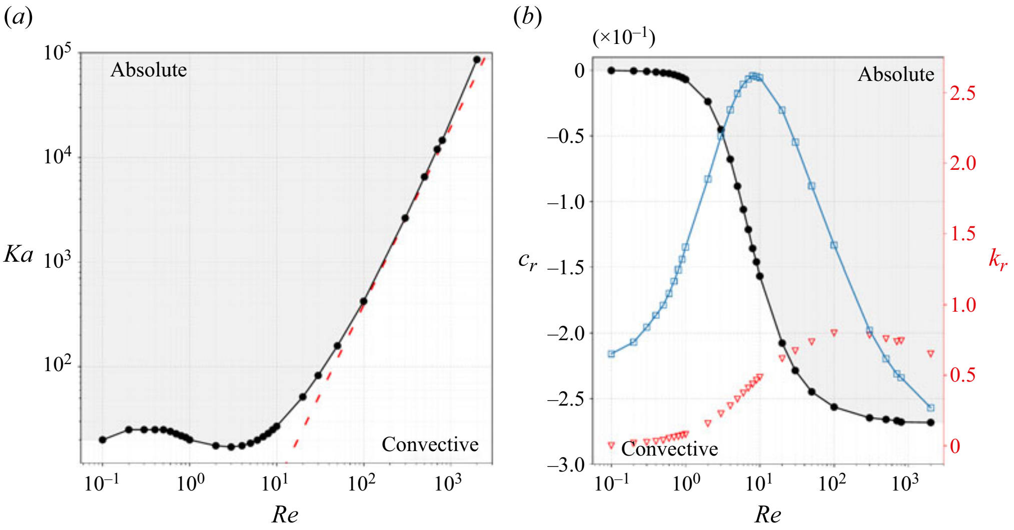

Figure 14. AC threshold (black dotted line) of the Derjaguin flat film solution ($\hat{h} = 1$) in (*a*) the *Ka*–*Re* space with the trend line $Ka = 0.15Re^{1.8}$ (red dashed line) and in (*b*) c_r–*Re* space with the associated real wavenumber k_r (red triangles) and non-dimensional capillary wavenumber k_{ℓ_c} (continuous blue line with blue squares).

c_r–*Re* space. For $Ka < 30$, the threshold has a minimum of $Ka = 17$ at $Re = 3$ and a maximum of $Ka = 25$ at $Re = 0.4$. For $Ka > 30$ and $Re \gtrsim 10$, it gets to an asymptote, which goes as $Ka \sim Re^{1.8}$ or in terms of capillary number as $Ca^{-1} \sim Re^{1.5}$. These results show that for fluids with $Ka < 17$, the Derjaguin solution is always convectively unstable regardless of the Reynolds number.

The neutral perturbations ($\omega_i = 0$) associated with the AC threshold have a negative phase speed for every *Re*. These travel faster than the substrate speed ($|c_r| > |U_p|$) for $Re \gtrsim 5.5$. The phase speed has a maximum at $Re = 0.1$ and an asymptote at c_r 2.7 for $Re > 300$. The real wavenumber k_r of the neutral perturbations has a maximum at $k_r \approx 0.8$ in the range $100 < Re < 200$. For $Re > 300$, k_r exceeds $\hat{\ell}_c$, highlighting how, at these wavelengths, surface tension starts to dominate over gravity.

5.3.2. *AC threshold in the* $\hat{h}$–*Re space for different Ka*

Moving to the AC threshold for the liquids in table 1, from figures 15–16 show the window of absolute instability in (*a*) the $\hat{h}$–*Re* space bounded by a lower and an upper threshold (black dots) and in (*b*) the c_r–*Re* space, with the real wavenumber k_r of the upper (red empty triangular markers) and lower thresholds (red empty circular markers). We also show a second AC upper threshold (green empty markers) and the LLD solution $\mathring{h}$ (dash-dotted orange line) for the water–glycerol ($Ka = 195$) solution and corn oil ($Ka = 4$). The absolute region's extrema and the upper threshold inflection points are reported in table 3.

For the four liquids, the lower threshold stems from $\hat{h} = 1$ as $Re \rightarrow 0$ and develops mainly in the thin film domain, with a minimum at intermediate *Re* values. The threshold extends into the thick film domain, with a plateau at $\hat{h} \approx 1.4$ for water–glycerol ($Ka = 195$) and corn oil ($Ka = 4$). The lower threshold of the corn oil extends solely into the thick film, with thin film base states ($\hat{h} < 1$) always convectively unstable. In the c_r–*Re* space, the neutral waves associated with the lower threshold travel upward against gravity ($c_r < 0$).

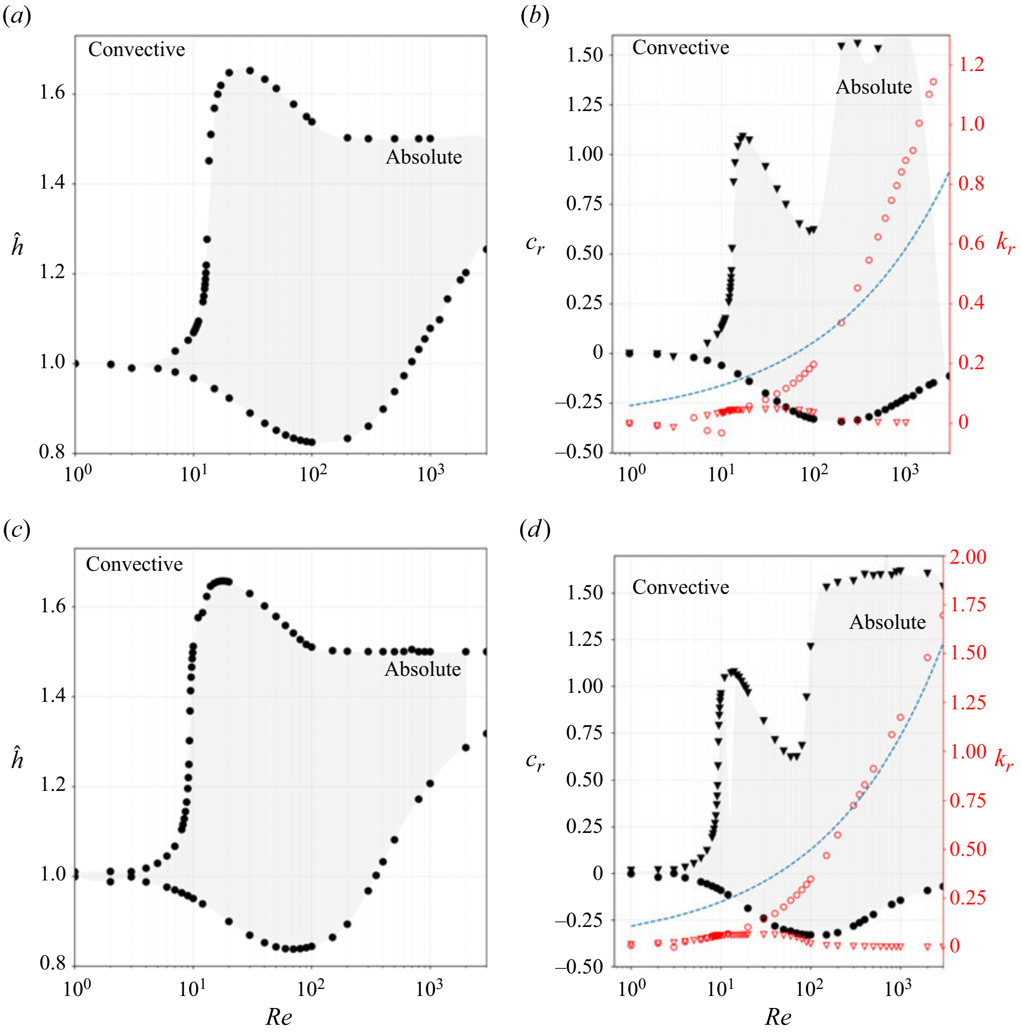

Figure 15. Upper and lower branches of the absolute instability region (black dots) in (*a*,*c*) the $\hat{h}$–Re and (*b*,*d*) c_r–Re spaces with the associated wavenumber k_r for the lower (circles) and upper (triangles) thresholds and the curve k_{ℓ_c} (dashed blue line) for (*a*,*b*) liquid zinc ($Ka = 11\,525$) and (*c*,*d*) water ($Ka = 3400$).

The associated wavenumber k_r monotonically increases with Re. Here k_r overtakes k_{ℓ_c} for the liquid zinc ($Ka = 11\,525$) and water, showing that the surface tension prevails over gravity for large Re. Due to surface tension effects, which support the entrainment action against gravity for intermediate Re, the minimum of the lower threshold $\hat{h}_{min}$ decreases with Ka, following the relations:

$$Re_{min} = 1.5496 Ka^{0.4677}, \quad \hat{h}_{min} = -0.0022 Re_{min} + 0.9403, \tag{5.25a,b}$$

where Re_{min} is the Re associated to $\hat{h}_{min}$.

The upper thresholds stem from $\hat{h} = 1$ and extend into the thick film domain ($\hat{h} > 1$) with a maximum of $\hat{h} \approx 1.65$ at $Re \approx 10$ and a plateau at $\hat{h} \approx 1.5$ for $Re > 100$. In the c_r–Re space, the neutral waves, associated with the upper threshold, travel downwards ($c_r > 0$) with a maximum at $Re \approx 1$ for corn oil ($Ka = 4$) and $Re \approx 100$ for the

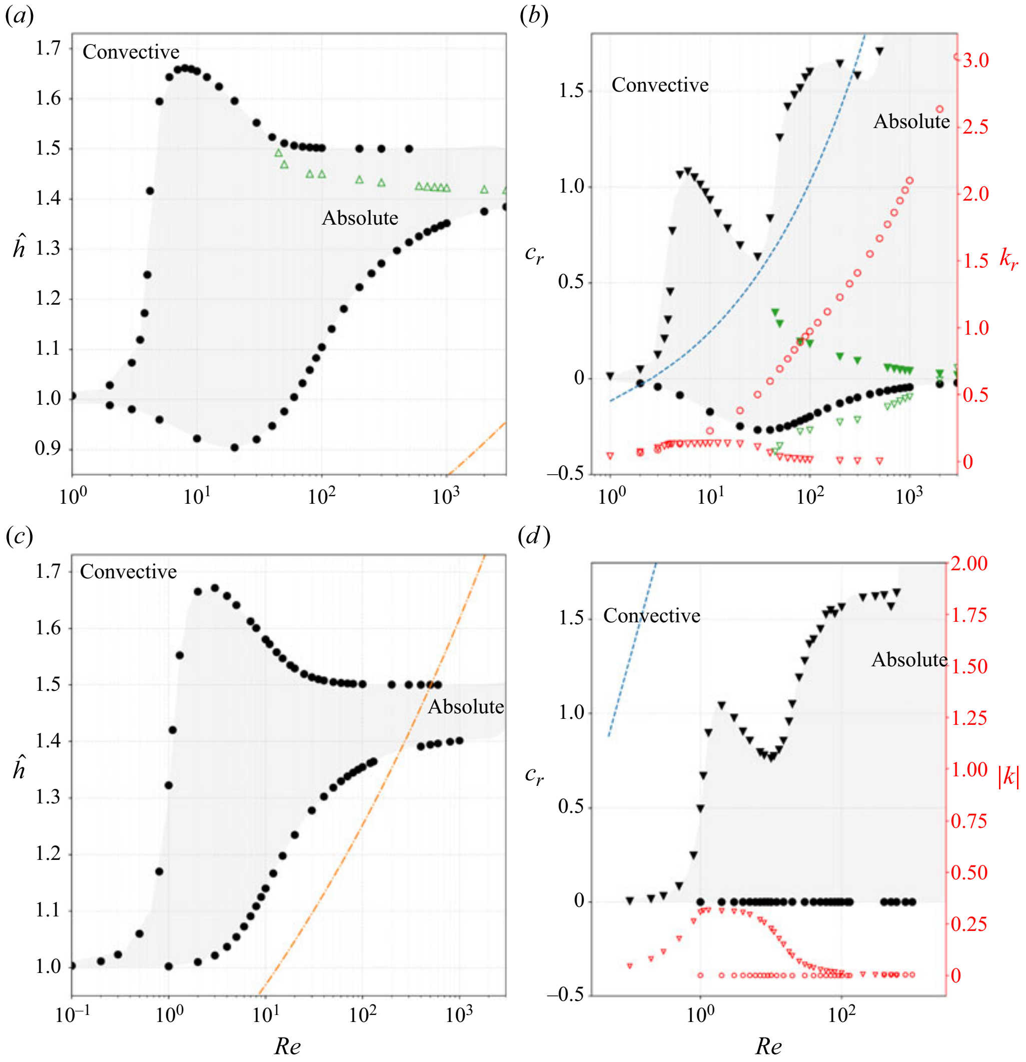

Figure 16. Upper and lower branches of the absolute instability region (black dots) in (*a*,*c*) the $\hat{h}$–*Re* space with the second branch of the upper threshold (green empty triangles) and the LLD solution (orange dash-dotted line) and in (*b*,*d*) the c_r–*Re* space with the associated wavenumber k_r for the lower (circles) and upper (triangles) thresholds and the curve k_{ℓ_c} (dashed blue line) for (*a*,*b*) water–glycerol ($Ka = 195$) and (*c*,*d*) corn oil ($Ka = 4$).

other liquids. As for the lower branch, based on the liquid's properties, we define the value of $\hat{h}_{max}$ and the associated *Re* (Re_{max}) as a function of *Ka* via the relations

$$Re_{max} = 1.9372Ka^{0.2732}, \quad \hat{h}_{max} = -0.0008Re_{max} + 1.6663. \qquad (5.26a,b)$$

Considering the operational range of the hot-dip galvanising process, using liquid zinc with $Re \in [437, 2273]$ and $\hat{h} < 0.2$, the flat liquid film is always convectively unstable.

In addition to the saddle point defining the upper branch, we found other valid saddle points for water–glycerol ($Ka = 195$). Figure 17 shows two saddle points (red circle and red square) (*a*) in the complex wavenumber space k_r–k_i with the ω_i colour map and

	Minimum				Maximum			
Ka	4	195	3400	11 525	4	195	3400	11 525
$\hat{h}_{min}$	—	0.904	0.838	0.824	0	1.661	1.658	1.658
Re_{min}	—	18.28	69.08	123.46	0	8.19	17.79	25

Table 3. Maximum and minimum of the absolute instability windows in the $\hat{h}$–Re space for different liquids.

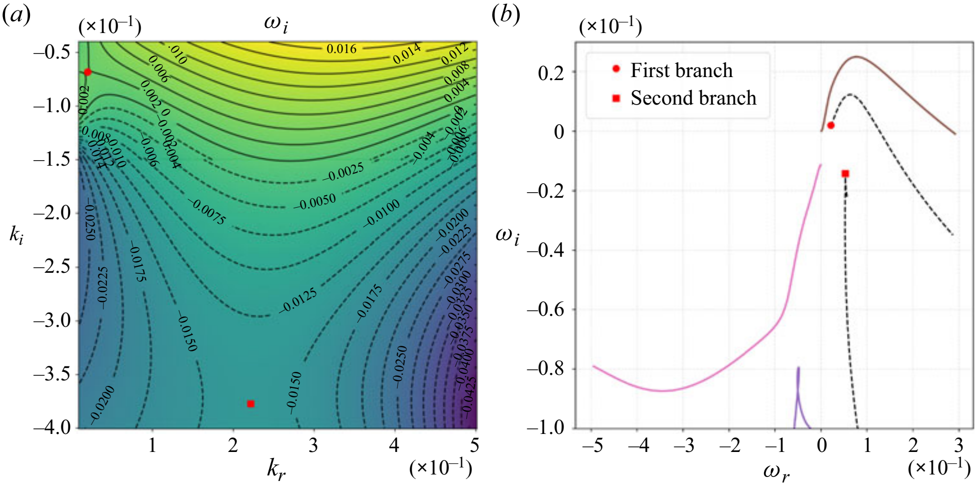

Figure 17. Position of two saddle points (red circle and red square) in (a) the k_r–k_i space with the ω_i colour plot and in (b) the ω_r–ω_i space with the temporal branches along the real wavenumber axis with $k_i = 0$ (continuous coloured lines) for water–glycerol ($Ka = 195$) with $\hat{h} = 1.48$ and $Re = 100$.

(b) in the complex frequency space ω_r–ω_i with the spatial branches along the real k axis with $k_i = 0$ for water–glycerol ($Ka = 195$) at $\hat{h} = 1.48$ and $Re = 100$. The two saddle points satisfy the collision criterion since an odd number of temporal branches surmount them. Based on the second saddle point (red square), which appears around $Re \approx 40$, we traced another AC threshold (green empty triangles in figure 16a). Interestingly, this threshold is always below the first and approaches the lower branch for larger Re, closing the window of absolute instability. This is also visible in the c_r–Re space (green triangles in figure 16b), where the phase speed of the two branches converges. Moreover, the wavenumber increases with Re reaching 0.5 for $Re = 3000$.

For $Re = 3000$, we discovered a collection of saddle points near the imaginary wavenumbers' axis. Figure 18 shows the position of six saddle points with (a,c) red markers in the k_r–k_i space with the ω_i colour map and with (b,d) coloured markers in the ω_r–ω_i space and the temporal branches along the real wavenumber axis (coloured lines) with $\hat{h} = 1.41$ and $Re = 3000$ for (a,b) water–glycerol ($Ka = 195$) and (c,d) $Ka = 0$. The first saddle point is used to construct the AC threshold described previously. For plotting convenience, we do not show the saddle point of the second upper branch because it is at a much larger real wavenumber. Only the first four of the six saddle points respect the collision criterion, with the first being the last to have a negative growth rate as we increase $\hat{h}$. Since the AC associated with this point represents the upper bound for the region of

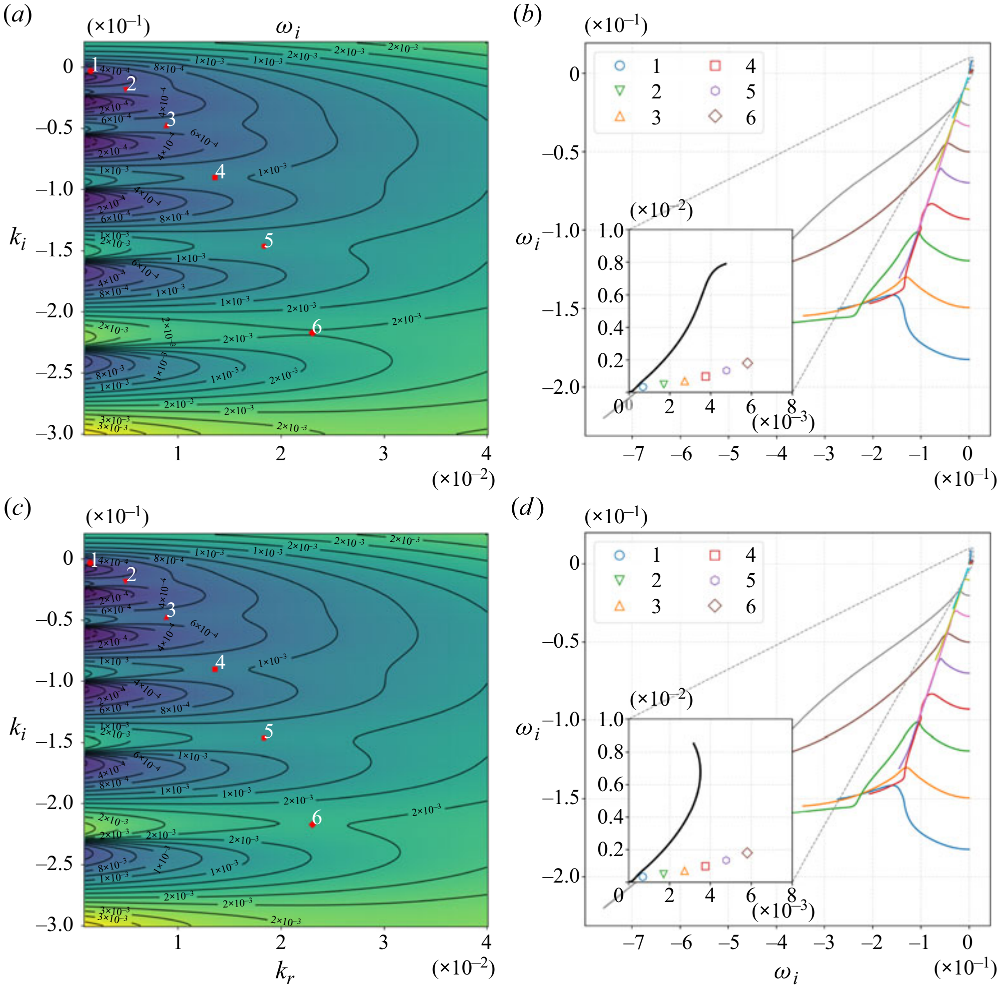

Figure 18. Multiple saddle points in (*a*,*c*) the complex wavenumber space k_r–k_i (numbered red markers) and (*b*,*d*) in the complex frequency domain ω_r–ω_i (empty coloured markers) with the temporal branches along the real wavenumber axis (coloured continuous line) at $Re = 3000$ and $\hat{h} = 1.41$ for (*a*,*b*) water–glycerol ($Ka = 195$) and (*c*,*d*) $Ka = 0$.

absolute stability, we did not investigate the AC for the other saddle points. The location of these saddle points is invariant with Ka since their positions are the same for the case with water–glycerol and $Ka = 0$. This implies that this part of the AC upper branch is not affected by the surface tension and is solely given by a balance of gravity and inertia.

The LLD solution $\mathring{h}$ (defined in (2.10)) is always convectively unstable for zinc ($Ka = 11\,525$), water ($Ka = 3400$) and water-glycerol ($Ka = 195$). For convenience, we did not report this curve for liquid zinc and water because it was much smaller $\hat{h}$ compared with the window of absolute instability. For corn oil ($Ka = 4$), $\mathring{h}$ crosses the area of absolute instability in the range $100 < Re < 500$. However, since this intersects the lower branch at a $Re \approx 300$, it is unrealistic to see it in an experiment. In addition, given that the wavenumber of the lower branch is tiny, this would require a very long domain for substrate velocities in the range $U_p \in [0.1–1]$ (m s^{-1}).

We rescale the upper and lower AC thresholds in the $\hat{h}$–Re space with $(\hat{h}_{max}, Re_{max})$ and $(\hat{h}_{min}, Re_{min})$, respectively, for liquid zinc ($Ka = 11\,525$), water ($Ka = 3400$) and water–glycerol ($Ka = 195$). Figure 19 shows the scaled (*a*,*b*) upper and (*c*,*d*) lower thresholds in (*a*,*c*) the $\hat{h}$–Re and (*c*,*d*) the $\check{h}$–Re spaces for the liquid zinc ($Ka = 11\,525$) (red circle), water ($Ka = 3400$) (blue squares) and water–glycerol ($Ka = 195$) (green triangles), where $\check{h}$ is the non-dimensional film thickness based on the viscous length ℓ_ν defined in (2.4). The curve matches perfectly apart from the lower bound in the $\hat{h}$–Re space at small and large Re. Moreover, we found a simple approximation to the lower AC threshold. Figure 19(*d*) shows a trend line (black loosely dashed line) for the lower branch, given by

$$\check{h}/\check{h}_{min} = (Re/Re_{min})^{4/9}. \tag{5.27}$$

This approximation enables the construction of the absolute instability window for any fluid within the range $Ka \in [195, 11\,525]$ without the need for further simulations.

6. Conclusion and perspectives

This study investigated the linear stability of a vertical liquid film over a substrate moving against gravity for four liquids with Ka numbers ranging from 4 to 11 525. We have identified the region of unstable perturbations by using long-wave asymptotic analysis and numerical solutions to the Orr–Sommerfeld eigenvalue problem. The instability mechanism has been described for the unstable solutions via momentum, vorticity and energy-based arguments, and the threshold between absolute and convective instability has been traced.

The neutral curves, growth rates and phase speed converge around the same values for $\hat{h} \gtrsim 0.7$, highlighting a stabilising mechanism where viscous effects balance gravitational effects with minimal influence from surface tension.

For thin films, the instability is driven by the amplitude of the vorticity with a minimal phase shift. For thick films, the amplitude decreases and the phase shift increases, with a peak shifted at larger k. The surface tension strongly affects this mechanism, simultaneously stabilising and destabilising the film, especially for $Ka = 11\,525$. For long waves, this curves the vorticity lines near the substrate, reducing the flow under the crests. For short waves, this enhances vorticity production at the free surface and creates a region of intense vorticity near the substrate.

Intense Reynolds stresses accompany areas of intense vorticity. At the same time, the dissipative terms also grow in magnitude, leading to two instability mechanisms for small and large Ka. For $Ka = 11\,525$, surface tension induces a larger vorticity production at the free surface and at the wall, resulting in significant Reynolds stresses and intense dissipative effects. In addition, the contribution to the viscous terms also increases. For $Ka = 4$ (corn oil), shear effects mainly influence the viscous term. The shear effects diminish for $Ka = 11\,525$ (zinc), and the extensional term becomes more important.

In terms of AC instability threshold, for $Ka < 17$ the LLD solution is always convectively unstable for any Re whereas for $Re \gtrsim 10$, the threshold follows an asymptote given by $Ka \approx 0.15\ Re^{1.8}$. In the $\hat{h}$–Re space, a window of absolute instability arises between the thin and thick film conditions. This window develops solely in the thick film region for $Ka = 4$ (corn oil). Moreover, a bifurcation point is also present at $Re \approx 40$, where two solution branches exist, one independent of Ka. Rescaling the lower (upper)

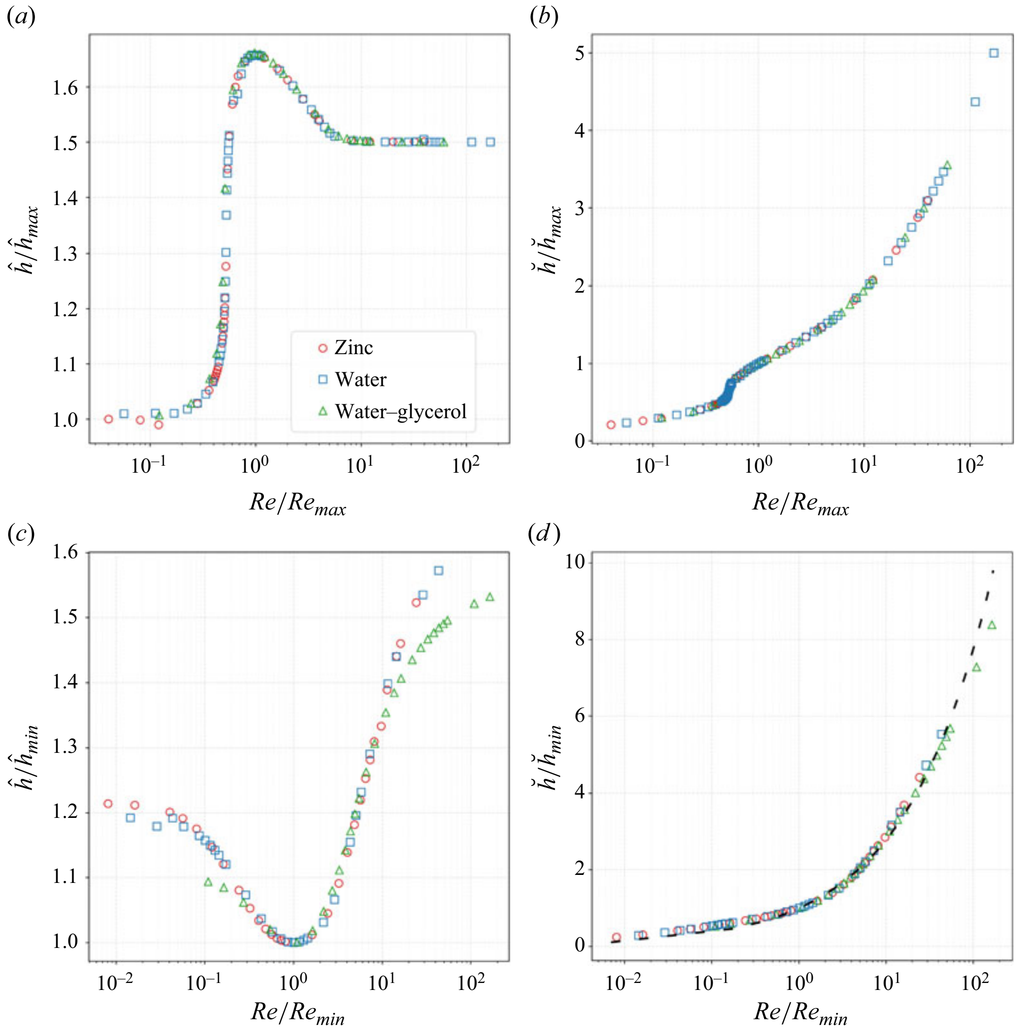

Figure 19. Scaled absolute instability window for liquid zinc ($Ka = 11\,525$; red circles), water ($Ka = 3400$; blue squares) and water-glycerol ($Ka = 195$; green triangles), with the (a,b) upper and (c,d) lower AC thresholds rescaled with their values at the maximum and the minimum in (a,c) the $\hat{h}$–Re and (b,d) the $\check{h}$–Re space with the trend line $\check{h}/\check{h}_{min} = (Re/Re_{min})^{4/9}$ (dashed black line).

branch of the absolute instability window with its minimum (maximum), the curves for $Ka > 4$ converge in the $\hat{h}$–Re space. A relation linking the value of Re at the minimum of this curve to the lower bound was also provided.

These findings provide crucial insights into the stability of the liquid film in dip-coating processes. Our analysis helps validate reduced-order models by comparing their predicted growth rates and neutral curves. By leveraging the numerical and analytical solutions of the Orr–Sommerfeld problem, we can develop optimal control strategies for external actuators to stabilise linearly unstable perturbations.

Future investigations could build on our findings by examining whether perturbations exhibit remnant behaviour, with waves propagating in both directions, as well as exploring transient growth mechanisms or transverse modulation due to nonlinear effects in three dimensions. Understanding instability mechanisms without external influences such as magnetic fields or airflow lays a solid foundation for more detailed studies incorporating these factors. Furthermore, direct numerical simulations could assess the accuracy of the AC threshold and uncover additional unstable saddle points in complex frequency space driven by nonlinear effects.

Funding. F.P. is supported by an F.R.S.-FNRS FRIA grant, and his PhD research project is funded by Arcelor-Mittal. B.S. is Research Director at F.R.S.-FNRS.

Declaration of interest. The authors report no conflict of interest.

Author ORCIDs.
Fabio Pino https://orcid.org/0000-0003-4970-1142;
Miguel A. Mendez https://orcid.org/0000-0002-1115-2187;
Benoit Scheid https://orcid.org/0000-0001-7268-581X.

Appendix A. Pseudocode for the search of the AC threshold

The pseudocode (Algorithm 1) reports the main steps of the AC threshold search. First, we define the liquid properties and the Kapitza number. Then we select a range of Reynolds numbers to calculate the threshold. Inside the 'for' loop, we choose one of these values and a guess value for $\hat{h}$, and we search for a valid saddle point in the complex wavenumber space. This procedure is done via trial and error. The wavenumbers space is explored in small windows until we find a saddle point. Then, we validate this point by visually inspecting two spatial branches from different half-planes pinch at the saddle point. If the saddle point is validated, we fix the window in the complex wavenumber space and define the limit for the $\hat{h}$ optimisation. We define the range of $\hat{h}$, such that the growth rate at the saddle point has a different value at the extremes of the range. Then we pass this information to a scalar optimisation algorithm that computes precisely the location of the threshold associated with a saddle point with $|\omega_i| < 10^6$. We store this value and move to another Re number. The procedure for the Ka–Re space is the same; instead of searching along $\hat{h}$, we search along Ka for a fixed Reynolds number.

Appendix B. Convergence study and code verification

Appendix B.1 reports the convergence study used to define a suitable number of Chebyshev polynomials in the solution of the Orr–Sommerfeld eigenvalue problem and the grid spacing of the complex wavenumber space in the AC threshold search. Appendix B.2 validates the numerical implementation, showing the eigenvalue spectrum obtained solving the Orr–Sommerfeld problem and the long-wave approximation of the Orr–Sommerfeld solution.

B.1. *Convergence study*

The values of the most-unstable eigenvalue are compared by varying the numbers of Chebyshev polynomials ($N = 10$, 20, 80 and 100) in the approximation of the eigenfunction $\varphi(\hat{y})$ for the liquid zinc with $Re = 20$, $\hat{h} = 1.7$ and $k = 10^{-2}$. Table 4 reports the real and imaginary part of the most-unstable eigenvalue and the difference in magnitude to the $N = 100$ case, expressed by the Euclidean norm. Ten polynomials are sufficient to approximate the unstable mode, with minor variation compared with the more-accurate $N = 100$ case. The solution with $N = 10$ guarantees an approximation error of at least 10^{-5} for both (*a*) the real and (*b*) the imaginary parts, also in terms

Algorithm 1 AC threshold search in the parameter space $\hat{h}$–Re.

```
function SCALAR OPTIMISATION($\boldsymbol{H}, \boldsymbol{K}, Re, Ka$)
    Select random value of $\hat{h}_r$ from $\boldsymbol{H}$
    Select the most-unstable mode at the border or the wavenumber window $\boldsymbol{K}$ solving the generalised eigenvalue problem
    Map the $\boldsymbol{K}$ into the frequency space with Rayleigh quotient iteration
    Calculate saddle point location with numerical differentiation
    Collect value of growth rate at the saddle point $\omega_{i_{SP}}$
    while $|\omega_{i_{SP}}| > 1 \times 10^{-6}$ do
        Select value of $\hat{h}_g$ from $\boldsymbol{H}$
        Map $\boldsymbol{K}$ into frequency space
        Compute saddle point location with numerical differentiation
        Check collision criterion
        Collect value of $\omega_i$ at the saddle point ($\omega_{i_{SP}}$)
    end while
    return $\hat{h}_g$
end function
Define liquid properties and $Ka$ number
Initialise list of $Re$ numbers: $\boldsymbol{a} = [Re_0, Re_1, \ldots, Re_N]$
Initialise empty list of $\hat{h}$: $\boldsymbol{b}$
for $n$ in (1,$N$) do
    Select Reynolds from the list $Re = \boldsymbol{a}[n]$
    Define guess value for $\hat{h} = \hat{h}_g$
    Search saddle point in wavenumber space
    Define limit of search window: $\boldsymbol{K} = [k_{r_{min}}, k_{i_{min}}, k_{r_{max}}, k_{r_{max}}]$
    Define limit for $\hat{h}$ line search: $\boldsymbol{H} = [\hat{h}_{min}, \hat{h}_{max}]$
    Compute $\hat{h}$ at the threshold $\hat{h}_n \leftarrow$SCALAR OPTIMISATION($\boldsymbol{H}, \boldsymbol{K}, Re, Ka$)
    Store $\boldsymbol{b} \leftarrow \hat{h}_n$
end for
```

of τ coefficients (reported in table 5). To be conservative and limit the linear system's size, we use $N = 20$ for the rest of the computations. In case matrix $\hat{A}$ used for the Rayleigh quotient iteration (3.4) is singular, we use $N = 30$ polynomials. Concerning the domain and grid spacing for the saddle point computation, we calculate the growth rate at the saddle point in $k_r \in [0.05, 0.1]$ and $k_i \in [-0.02, 0.04]$, testing three different meshes: $M \times M = \{100 \times 100, 200 \times 200, 500 \times 500\}$. Table 6 reports the value of k_r and k_i at the saddle point and the associated ω_i. A grid of $M \times M = 200 \times 200$ is sufficient to have an accuracy of the growth rate up to the sixth digit, compared with the $M \times M = 500 \times 500$ case. Therefore, a $M \times M = 200 \times 200$ grid is a good compromise between results accuracy and computational cost. This grid spacing corresponds to a discretisation step of $\Delta k_r = 2.5 \times 10^{-4}$ and $\Delta k_i = 3 \times 10^{-4}$, which are used for the saddle point search.

B.2. *Verification*

To verify the numerical implementation, we compare the growth rate and the eigenfunction obtained with the spectral method (with $N = 20$) against a long-wave asymptotic

N	ω_r	ω_i	Accuracy
10	1.61898344	0.4042714	1.5299×10^{-4}
20	1.61898354	0.40427141	1.5308×10^{-4}
80	1.61897484	0.40429792	1.5322×10^{-4}
100	1.6188345	0.40423644	—

Table 4. Values of ω_i and ω_r of the most-unstable eigenvalue (largest ω_i) for $Re = 20$, $\hat{h} = 1.7$ and $k = 10^{-2}$ for four different numbers of Chebyshev polynomials N with their relative accuracy expressed as the Euclidean norm of the eigenvalue difference with respect to the $N = 100$ case.

N	τ_1	τ_2	τ_3	τ_4
10	$(3 - 4i) \times 10^{-6}$	$(-0.5 + i) \times 10^{-6}$	$(0.5 - 2i) \times 10^{-7}$	$(-0.3 + i) \times 10^{-8}$
20	$(-1 - 2i) \times 10^{-14}$	$(-1 - 9i) \times 10^{-15}$	$(0.8 - i) \times 10^{-15}$	$(-4 - 6i) \times 10^{-15}$
80	$(0.6 + i) \times 10^{-10}$	$(3 + i7) \times 10^{-11}$	$(1 - i) \times 10^{-11}$	$(4 + i4) \times 10^{-12}$
100	$(2 + i4) \times 10^{-10}$	$(-5 + i0.1) \times 10^{-7}$	$(0.5 + i2) \times 10^{-7}$	$(0.3 + i1.2) \times 10^{-8}$

Table 5. Values of the τ coefficients estimating the approximation error for four different numbers of Chebyshev polynomials N in the case of liquid zinc with $Re = 20$, $\hat{h} = 1.7$ and $k = 1 \times 10^{-2}$.

$M \times M$	k_r	k_i	ω_i
100×100	0.0778	0.0176	0.00056017
200×200	0.0776	0.0174	0.0005594
500×500	0.0778	0.0173	0.0005599

Table 6. Position of the saddle point in the complex wavenumber space (k_r–k_i) and the associated growth rate ω_i, for three mesh sizes M using liquid film with $Re = 30$ and $\hat{h} = 0.9$.

expansion, obtained approximating the solution $(\varphi(\hat{y}), c)$ with a power series, up to third order, of $k \in \mathbb{R}$ (Yih 1963):

$$\varphi(\hat{y}) = \varphi_0(\hat{y}) + \varphi_1(\hat{y})k + \varphi_2(\hat{y})k^2 + \varphi_3(\hat{y})k^3 + O(k^4), \tag{B1a}$$

$$c = c_0 + c_1 k + c_2 k^2 + c_3 k^3 + O(k^4), \tag{B1b}$$

with the long-wave assumption

$$k \ll 1 \quad \text{and} \quad Re = O(1). \tag{B2a,b}$$

Injecting (B1) into (2.19) and (2.22) and solving for $O(1)$ leads to the leading-order solution:

$$\varphi_0(\hat{y}) = \hat{y}^2, \quad c_0 = (\hat{h}^2 - 1). \tag{B3a,b}$$

In the calculation, we assumed for convenience that the constant associated with $\hat{y}^2$ is equal to unity (Kalliadasis *et al.* 2011, Subsection 3.5.3), which is equivalent to setting the liquid film's displacement amplitude to two ($\eta = 2$). This solution corresponds to the displacement of the film thickness associated with a variation of the flow rate with a simply advected perturbation, which is neither amplified nor damped. In the liquid-film-stability literature, this is known as the Goldstone mode (Colinet, Legros & Velarde 2001). In our case, the magnitude and direction of the phase speed depend on $\hat{h}$. Waves have a zero phase speed for $\hat{h} = 1$. For $\hat{h} < 1$, waves propagate upwards and for $\hat{h} > 1$, waves propagate in

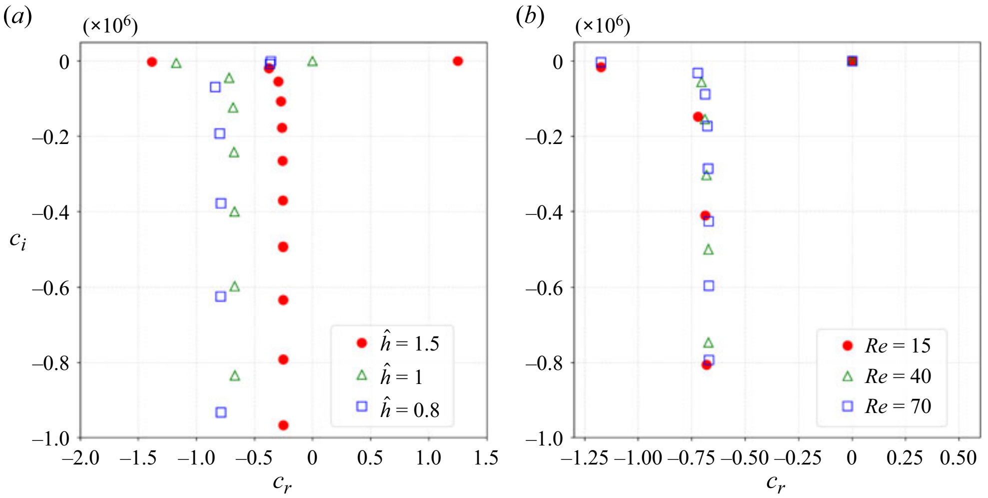

Figure 20. Spectrum of the Orr–Sommerfeld operator obtained using 80 Chebyshev polynomials considering liquid zinc and $k = 10^{-5}$ (*a*) for different values of the liquid-film height $\hat{h}$ with $Re = 50$ and (*b*) for different values of Re with $\hat{h} = 1$.

the direction of the gravitational acceleration, with waves going faster in magnitude than any other particle inside the base flow ($c > 1$) for $\sqrt{2} < \hat{h} < \sqrt{3}$.

The spectral method accurately predicts this leading-order solution. Figure 20 shows the spectrum of the eigenvalue problem for $k = 10^{-5}$ (*a*) for different $\hat{h}$ with $Re = 50$ and (*b*) for different Re with $\hat{h} = 1$. The spectrum presents two discrete eigenvalues; that with the largest c_r corresponds to the Goldstone mode. The spectrum also presents a continuous branch of eigenvalues in the negative c_r plane. As $\hat{h}$ increases, the discrete eigenvalues tend to spread on the real axis, whereas the continuous branch approaches the imaginary axis. As Re decreases, the continuous spectrum spreads along the imaginary axis. While the left eigenvalue tends to spread along the negative real axis, the Goldstone mode does not move, in agreement with the asymptotic expansion.

Moving to higher-order terms in the asymptotic expansion, the solution at $O(k)$ is given by an imaginary streamwise velocity $\varphi_1(\hat{y})$ and an imaginary phase speed c_1:

$$\varphi_1(\hat{y}) = \mathrm{i}\frac{1}{60}(\hat{h}\,Re\,\hat{y}^5 - 5\hat{h}^2\,Re\,\hat{y}^4), \quad c_1 = \mathrm{i}\frac{2}{15}\hat{h}^6 Re. \qquad \text{(B4}a,b\text{)}$$

In the derivation, we set the quadratic term $\hat{y}^2$ to zero such that (B4) represents a pure higher-order polynomial correction to the leading-order solution $\varphi_0(\hat{y})$ (Kalliadasis *et al.* 2011, § 3.5.3). In the phase speed, the sixth-power dependence on $\hat{h}$ highlights the critical effect of the liquid-film height even at small k.

We can include the surface tension effect at this order, assuming $(Ca^{-1} \times k^2) = O(1)$ (Pelisson Chimetta *et al.* 2018). This leads to the corrected solution:

$$\varphi_1^\star(\hat{y}) = \frac{\mathrm{i}}{60}(\hat{h}\,Re\,\hat{y}^5 - 5\hat{h}^2\,Re\,\hat{y}^4 + 20k^2\,Ca^{-1}\,\hat{y}^3), \quad c_1^\star = \frac{\mathrm{i}}{15}(2\hat{h}^6\,Re - 5\hat{h}^3 k^2\,Ca^{-1}). \qquad \text{(B5}a,b\text{)}$$

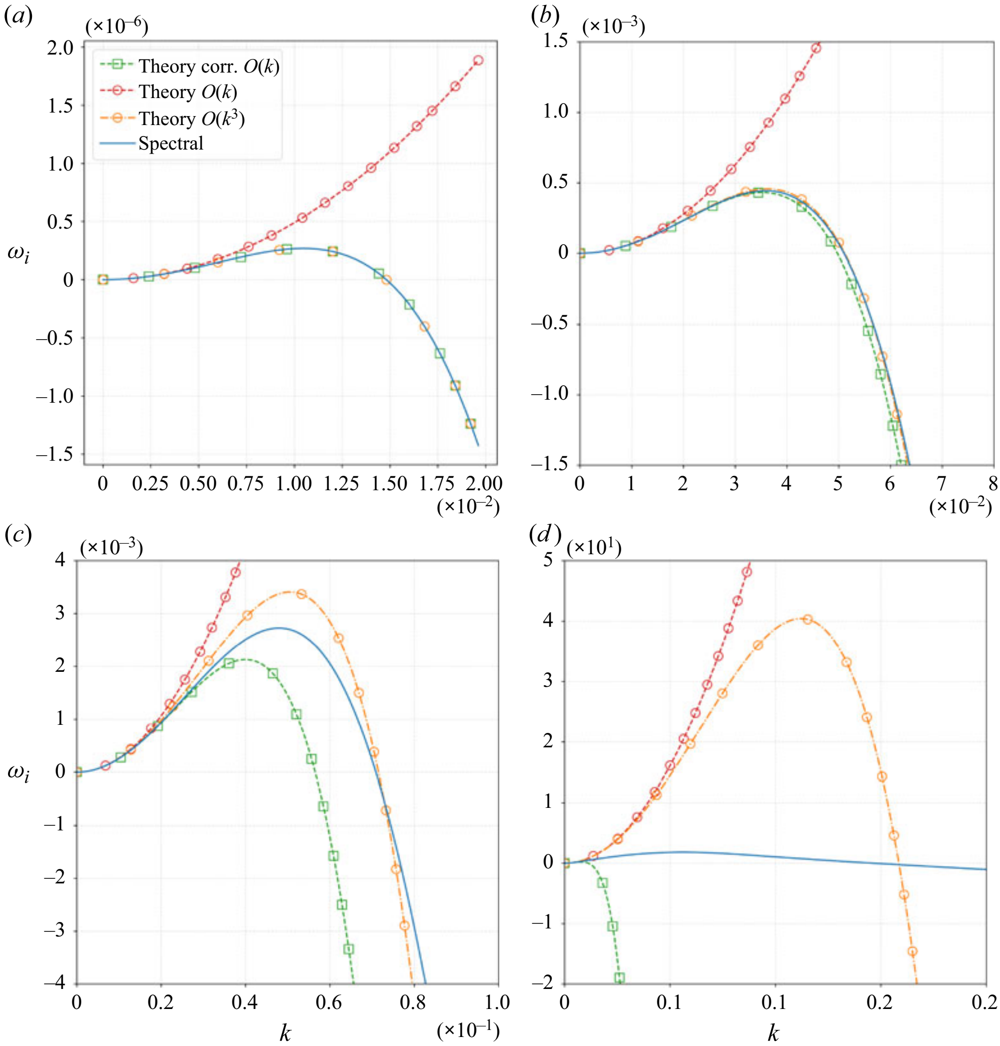

Figure 21. Comparison of the growth rate ω_i between long-wave expansion up to $O(k^3)$ (dash-dotted orange line with circles), up to $O(k)$ with (dashed green line with squares) and without (dashed red line with squares) surface tension correction and the result obtained with the spectral method (continuous blue line) considering liquid zinc with $Re = 20$ for (*a*) $\hat{h} = 0.35$, (*b*) $\hat{h} = 0.8$, (*c*) $\hat{h} = 1$ and (*d*) $\hat{h} = 1.7$.

For the higher-order term solutions, we neglect the hypothesis on the surface tension, which then appears starting at $O(k^3)$ (Benney 1966). The solution at $O(k^2)$ reads

$$\varphi_2(\hat{y}) = \frac{\hat{y}^3(\hat{h}(Re^2\hat{y}(224\hat{h}^5 - 56\hat{h}^3\hat{y}^2 + 32\hat{h}^2\hat{y}^3 - 9\hat{h}\hat{y}^4 + \hat{y}^5) + 6720) + 3360\hat{y})}{20160}, \quad \text{(B6a)}$$

$$c_2 = \frac{\hat{h}^4}{63}(4\hat{h}^6 Re^2 + 63), \quad \text{(B6b)}$$

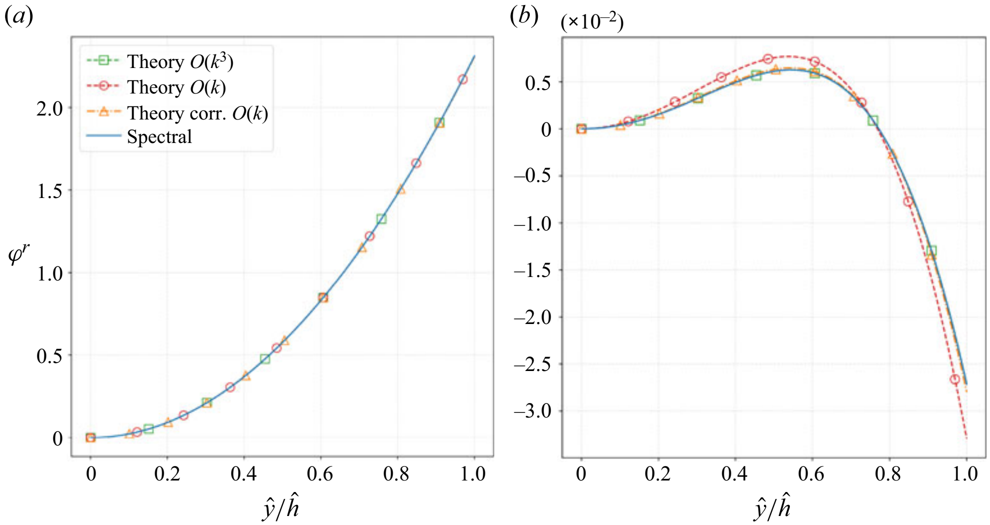

Figure 22. Comparison of the eigenfunction $\varphi(\hat{y})$ considering liquid zinc with $\hat{h} = 1.3$, $Re = 10$ and $k = 0.02$ between the long-wave expansions up to $O(k)$ (dashed orange line with triangle markers), to $O(k)$ with surface tension correction (dotted green line with square markers) and to $O(k^3)$, against the solution of the Orr–Sommerfeld problem with $N = 20$ Chebyshev polynomials (continuous blue line) in terms of the (*a*) real and (*b*) imaginary parts.

and at $O(k^3)$ reads

$$\begin{aligned}\varphi_3(\hat{y}) = -\Bigg(&\frac{\mathrm{i}\hat{y}^3(-17160\,Re\,\hat{y}^5(\hat{h}^6\,Re^2-12)-27456\hat{h}\,Re\,\hat{y}^4(8\hat{h}^6\,Re^2+45)+51480\hat{h}^5\,Re^3\,\hat{y}^6)}{1037836800}\\ &+\frac{+\mathrm{i}\hat{y}^3(5765760(13\hat{h}^5\,Re-60Ca^{-1})-26884\hat{h}^4\,Re^3\,\hat{y}^7+7904\hat{h}^3\,Re^3\,\hat{y}^8)}{1037836800}\\ &+\frac{+\mathrm{i}\hat{y}^3(17297280\hat{h}^3\,Re\,\hat{y}^2-1365\hat{h}^2\,Re^3\,\hat{y}^9-1372800\hat{h}^4\,Re\,\hat{y}(4\hat{h}^6\,Re^2+63))}{1037836800}\\ &+\frac{\mathrm{i}\hat{y}^3(192192\hat{h}^2\,Re\,\hat{y}^3(4\hat{h}^6\,Re^2+15)+105\hat{h}\,Re^3\,\hat{y}^{10})}{1037836800}\Bigg),\end{aligned} \tag{B7a}$$

$$c_3 = -\frac{75872\mathrm{i}\hat{h}^{14}\,Re^3}{2027025} - \frac{157}{224}\,\mathrm{i}\hat{h}^8 Re - \frac{1}{3}\mathrm{i}\hat{h}^3 Ca^{-1}. \tag{B7b}$$

Figure 21 shows a comparison of the growth rates ($\omega_i = kc_i$) of the most-unstable mode for the expansion up to $O(k^3)$ (orange dash-dotted line with circles), up to $O(k)$ with (green dashed line with circles) and without (red dashed line with circles) surface tension correction and that obtained with the spectral method (continuous blue line) at $Re = 20$ with liquid zinc's properties for (*a*) $\hat{h} = 0.35$, (*b*) $\hat{h} = 0.8$, (*c*) $\hat{h} = 1$ and (*d*) $\hat{h} = 1.7$. The numerical results agree with the three expansions for $k \to 0$.

For $\hat{h} = 0.35$ the solutions at $O(k^3)$, at $O(k)$ with correction and the spectral one match for all k with the solution at $O(k)$ diverging around $k = 0.75 \times 10^{-2}$. As $\hat{h}$ increases, the curves start to disagree for larger k. At $\hat{h} = 1$, the solution at $O(k^3)$ predicts very well the cutoff wavenumber (where $\omega_i = 0$), despite overpredicting the location and the magnitude of the growth rate peak. At $\hat{h} = 1.7$, the asymptotic solutions completely disagree with the Orr–Sommerfeld solution as the range of unstable wavenumbers enlarges and the long-wave assumption loses validity. These results verify the numerical implementation and highlight the long-wave nature of the instability for $\hat{h} \to 0$.

The agreement between theory and numerics is also evident in terms of eigenfunctions. Figure 22 shows the comparison of the eigenfunction associated with the most-unstable mode at $\hat{h} = 1.3$, $k = 0.02$ and $Re = 20$ for both (*a*) the real and (*b*) the imaginary parts, scaled with the normalisation constraint:

$$\int_0^{\hat{h}} \varphi(\hat{y})\, \mathrm{d}\hat{y} = 1. \tag{B8}$$

Both the real and the imaginary parts agree perfectly for all the expansions and the spectral results, apart from the solution at $O(k)$, which overpredicts the peak in the imaginary part and a small deviation for $\hat{y} \to \hat{h}$.

In conclusion, given the agreement of both the growth rates and the eigenfunction, we consider the numerical implementation verified.

REFERENCES

AVANCI, M.P, RODRÍGUEZ, D. & ALVES, L.S.DEB. 2019 A geometrical criterion for absolute instability in separated boundary layers. *Phys. Fluids* **31** (1), 014103.

BARREIRO-VILLAVERDE, D., GOSSET, A., LEMA, M. & MENDEZ, M.A. 2023 Damping of three-dimensional waves on coating films dragged by moving substrates. *Phys. Fluids* **35** (7), 072110.

BENJAMIN, T.B. 1957 Wave formation in laminar flow down an inclined plane. *J. Fluid Mech.* **2** (6), 554–573.

BENNEY, D.J. 1966 Long waves on liquid films. *Journal of mathematics and physics* **45** (1–4), 150–155.

BOURNE, D. 2003 Hydrodynamic stability, the Chebyshev tau method and spurious eigenvalues. *Contin. Mech. Thermodyn.* **15**, 571–579.

BOYD, J.P. 2001 *Chebyshev and Fourier Spectral methods*. Courier Corporation.

BREVDO, L., LAURE, P., DIAS, F. & BRIDGES, T.J. 1999 Linear pulse structure and signalling in a film flow on an inclined plane. *J. Fluid Mech.* **396**, 37–71.

BRIGGS, R.J. 1964 *Electron-stream Interaction With Plasmas*vol. 187. MIT Press.

BRUN, P-T., DAMIANO, A., RIEU, P., BALESTRA, G. & GALLAIRE, F. 2015 Rayleigh–Taylor instability under an inclined plane. *Phys. Fluids* **27** (8), 084107.

BUCHLIN, J.M. 1997 Modeling of gas-jet wiping. In *Thin Liquid Films and Coating Processes*, VKI Lecture Series. von Kármán Institute for Fluid Dynamics, Belgium.

CANUTO, C., HUSSAINI, M.Y., QUARTERONI, A., THOMAS, A., Jr. 2012 *Spectral Methods in Fluid Dynamics*. Springer Science & Business Media.

CHARRU, F. 2011 *Hydrodynamic Instabilities*, vol. 37. Cambridge University Press.

COLINET, P., LEGROS, J.C. & VELARDE, M.G. 2001 *Nonlinear Dynamics of Surface-Tension-Driven Instabilities*, vol. 527. Wiley Online Library.

DAWKINS, P.T., DUNBAR, S.R. & DOUGLASS, R.W. 1998 The origin and nature of spurious eigenvalues in the spectral tau method. *J. Comput. Phys.* **147** (2), 441–462.

DERJAGUIN, B.V. 1943 On the thickness of the liquid film adhering to the walls of a vessel after emptying. *Acta Physicochim. URSS* **20**, 349–352.

DERJAGUIN, B.V.C.R. 1944 On the thickness of the liquid film adhering to the walls of a vessel after emptying. *Prog. Surf. Sci.* **43** (1–4), 134–137.

DIETZE, G.F., AL-SIBAI, F. & KNEER, R. 2009 Experimental study of flow separation in laminar falling liquid films. *J. Fluid Mech.* **637**, 73–104.

GARDNER, D.R., TROGDON, S.A. & DOUGLASS, R.W. 1989 A modified tau spectral method that eliminates spurious eigenvalues. *J. Comput. Phys.* **80** (1), 137–167.

GASTER, M. 1968 Growth of disturbances in both space and time. *Phys. Fluids* **11** (4), 723–727.

GOSSET, A. & BUCHLIN, J.-M. 2006 Jet wiping in hot-dip galvanization. *J. Fluids Engng* **129** (4), 466–475.

GOSSET, A., MENDEZ, M.A. & BUCHLIN, J.-M. 2019 An experimental analysis of the stability of the jet wiping process. Part I. Characterization of the coating uniformity. *Exp. Therm. Fluid Sci.* **103**, 51–65.

GOSSET, A.M. 2007 Study of the interaction between a gas flow and a liquid film entrained by a moving surface (unpublished doctoral dissertation). PhD thesis, Université Libre de Bruxelle.

HUERRE, P. & MONKEWITZ, P.A. 1985 Absolute and convective instabilities in free shear layers. *J. Fluid Mech.* **159**, 151–168.

IVANOVA, T., PINO, F., SCHEID, B. & MENDEZ, M.A. 2022 Evolution of waves in liquid films on moving substrates. arXiv:2203.08201

JOHNSON, D. 1996 Chebyshev polynomials in the spectral tau method and applications to eigenvalue problems. *NASA Tech. Rep.*. National Aeronautics and Space Administration (NASA).

JOSE, A., PAREEK, S. & RADHAKRISHNAN, E.K. 2020 Advances in edible fruit coating materials. *Advances in Agri-food Biotechnology* (ed. T.R. Sharma, R. Deshmukh & H. Sonah), pp. 391–408. Springer Singapore.

KALLIADASIS, S., RUYER-QUIL, C., SCHEID, B., VELARDE, M.G. 2011 *Falling Liquid Films*, vol. 176. Springer Science & Business Media.

KELLY, R.E., GOUSSIS, D.A., LIN, S.P. & HSU, F.K. 1989 The mechanism for surface wave instability in film flow down an inclined plane. *Phys. Fluids* A*: Fluid Dyn.* **1** (5), 819–828.

KUKLÍK, V. & KUDLACEK, J. 2016 *Hot-dip Galvanizing of Steel Structures*. Butterworth-Heinemann.

KUPFER, K., BERS, A. & RAM, A.K. 1987 The cusp map in the complex-frequency plane for absolute instabilities. *Phys. Fluids* **30** (10), 3075–3082.

LANCZOS, C. 1988 *Applied Analysis*. Courier Corporation.

LANDAU, L. & LEVICH, B 1988 Dragging of a liquid by a moving plate. In *Dynamics of Curved Fronts*, pp. 141–153. Elsevier.

LEDDA, P.G., BALESTRA, G., LERISSON, G., SCHEID, B., WYART, M. & GALLAIRE, F. 2021 Hydrodynamic-driven morphogenesis of karst draperies: spatio-temporal analysis of the two-dimensional impulse response. *J. Fluid Mech.* **910**, A53.

LIGHTHILL, M.J. 1963 *Introduction Boundary Layer Theory*. Oxford University Press.

LIN, S.P. 1970 Roles of surface tension and Reynolds stresses on the finite amplitude stability of a parallel flow with a free surface. *J. Fluid Mech.* **40** (2), 307–314.

LIN, S.P., LIAN, Z.W. & CREIGHTON, B.J. 1990 Absolute and convective instability of a liquid sheet. *J. Fluid Mech.* **220**, 673–689.

LIU, J., PAUL, J.D. & GOLLUB, J.P. 1993 Measurements of the primary instabilities of film flows. *J. Fluid Mech.* **250**, 69–101.

MENDEZ, M.A., GOSSET, A., SCHEID, B., BALABANE, M. & BUCHLIN, J.-M. 2021 Dynamics of the jet wiping process via integral models. *J. Fluid Mech.* **911**, A47.

MORTON, B.R. 1984 The generation and decay of vorticity. *Geophys. Astrophys. Fluid Dyn.* **28** (3–4), 277–308.

ORTIZ, E.L. 1969 The tau method. *SIAM J. Numer. Anal.* **6** (3), 480–492.

PELISSON CHIMETTA, B., HOSSAIN, M.Z. & DE MORAES FRANKLIN, E. 2018 Numerical solution for Kapitza waves on a thin liquid film. *J. Braz. Soc. Mech. Sci. Engng* **40** (8), 1–11.

PIER, B. 2003 Open-loop control of absolutely unstable domains. *Proc. R. Soc. Lond.* A*: Math. Phys. Engng Sci.* **459** (2033), 1105–1115.

PINO, F., MENDEZ, M.A. & SCHEID, B. 2024 Absolute and convective instabilities in a liquid film over a substrate moving against gravity. *Phys. Rev. Fluids* **9** (10), 104002.

PINO, F., SCHEID, B. & MENDEZ, M.A. 2024 Absolute/convective instability threshold in inverted falling film through linear stability analysis. In *AIP Conference Proceedings*, vol. 3094. AIP Publishing.

SCHEID, B., KOFMAN, N. & ROHLFS, W. 2016 Critical inclination for absolute/convective instability transition in inverted falling films. *Phys. fluids* **28** (4), 044107.

SCHMID, P.J., HENNINGSON, D.S. & 2002 *Stability and transition in shear flows. Applied Mathematical Sciences, Vol. 142* Springer-Verlag.

SCRIVEN, L.E. 1988 Physics and applications of dip coating and spin coating. *MRS Online Proc. Library (OPL)* **121**, 717.

SHARMIN, E., ZAFAR, F., AKRAM, D., ALAM, M. & AHMAD, S. 2015 Recent advances in vegetable oils based environment friendly coatings: a review. *Ind. Crops Prod.* **76**, 215–229.

SMITH, M.K. 1990 The mechanism for the long-wave instability in thin liquid films. *J. Fluid Mech.* **217**, 469–485.

SNOEIJER, J.H., ZIEGLER, J., ANDREOTTI, B., FERMIGIER, M. & EGGERS, J. 2008 Thick films of viscous fluid coating a plate withdrawn from a liquid reservoir. *Phys. Rev. Lett.* **100**, 244502.

STERMAN-COHEN, E., BESTEHORN, M. & ORON, A. 2017 Rayleigh–Taylor instability in thin liquid films subjected to harmonic vibration. *Phys. Fluids* **29** (5), 052105.

SUHAG, R., KUMAR, N., PETKOSKA, A.T. & UPADHYAY, A. 2020 Film formation and deposition methods of edible coating on food products: a review. *Food Res. Intl* **136**, 109582.

SUSLOV, S.A. 2006 Numerical aspects of searching convective/absolute instability transition. *J. Comput. Phys.* **212** (1), 188–217.

THUAL, S., THUAL, O. & DEWITTE, B. 2013 Absolute or convective instability in the equatorial Pacific and implications for ENSO. *Q. J. R. Meteorol. Soc.* **139** (672), 600–606.

TREFETHEN, L.N. & BAU, D. 2022 *Numerical Linear Algebra*, vol. 181. SIAM.

TU, C.V. & ELLEN, C.H. 1986 Stability of liquid coating in the jet stripping process. In *9th Australasian Fluid Mechanics Conference*, Auckland, New Zealand, 8–12 December. University of Auckland.

WEINSTEIN, S.J. & RUSCHAK, K.J. 2004 Coating flows. *Annu. Rev. Fluid Mech.* **36**, 29–53.

WILSON, S.D.R. 1982 The drag-out problem in film coating theory. *J. Engng Math.* **16** (3), 209–221.

WU, J.-Z. 1995 A theory of three-dimensional interfacial vorticity dynamics. *Phys. Fluids* **7** (10), 2375–2395.

YIH, C.-S. 1963 Stability of liquid flow down an inclined plane. *Phys. Fluids* **6** (3), 321–334.

YIH, C.-S. 1991 Stability of liquid flow down an inclined plane. *Selected Papers By Chia-Shun Yih: (In 2 Volumes)*, 357 370. World Scientific.